SCIEPublish

Article

The Crystallography of Diverse Intermetallic Phases in Binary La-Ni Alloy Obtained by Melting and Its Structural Evolution under High Temperature Sintering

Yibo Liu [1,†], Tenghui Ren [1,†], Bin Wen [1], Zhefeng Xu [1,2], Yuefeng Wang [1], Changzeng Fan [1,2,*] and Lifeng Zhang [1,3,*]

[1] State Key Laboratory of Metastable Materials Science and Technology, Yanshan University, Qinhuangdao 066004, China; 202121020059@stumail.ysu.edu.cn (Y.L.); RTenghui@163.com (T.R.); wenbin@ysu.edu.cn (B.W.); zfxu@ysu.edu.cn (Z.X.); wangyuefeng@ysu.edu.cn (Y.W.)

[2] Hebei Key Lab for Optimizing Metal Product Technology and Performance, Yanshan University, Qinhuangdao 066004, China

[3] School of Mechanical and Materials Engineering, North China University of Technology, Beijing 100144, China

* Corresponding author. E-mail: chzfan@ysu.edu.cn (C.F.); zhanglifeng@ncut.edu.cn (L.Z.)

† These authors contribute equally.

Received: 24 July 2025; Accepted: 27 August 2025; Available online: 2 September 2025

ABSTRACT: In this study, we have investigated the structural evolution of binary La-Ni alloy under different heat treatments by combing single crystal X-ray diffraction (SXRD) as well as scanning electron microscope (SEM) and transmission electron microscopy (TEM). It has been found that LaNi and La_7Ni_3 can be successfully synthesized through the arc melting method. Then it was found that $LaNi_5$ appears in the binary La-Ni mixture wrapped by a Tantalum sheet, followed by high-temperature sintering. Next, some pilot experiments have been carried out on the La-Ni mixture by sealing tube technique with some residual oxygen. Serendipitously, oxidation has not been found while $La_3Ni_3Si_2$ and La_2NiSi besides LaNi phase show up. Meanwhile, the detailed crystal structure information and their topological features of the aforementioned phases as well as their high-resolution TEM images, have been obtained. Furthermore, the orientation relationships of the Si-contaminated mixed phases have been thoroughly investigated by advanced precession images of SXRD patterns.

Keywords: LaNi; La_7Ni_3; $LaNi_5$; $La_3Ni_3Si_2$; La_2NiSi; Single crystal; Crystal structure; Orientation relationship

1. Introduction

The study of intermetallic compounds, especially those involving rare earth elements, has attracted much attention due to their interesting magnetic, electrical, and structural properties [1–3]. For instance, the recently reported La-F-Se compounds exhibit exceptional electronic characteristics [4,5]. Notably, the La-Ni system and the La-Ni-Si ternary system have been identified as promising materials for various applications, including hydrogen storage alloys [6–10], battery electrodes [11], thermoelectric materials [12], superconducting materials [13–18], and catalytic materials [19–21].

The La-Ni binary alloy system contains numerous compounds of various types and proportions, which have been thoroughly explored and extensively researched. These different ratios contribute to the diverse performance characteristics of the alloys. Buschow and Yamamoto synthesized a series of La-Ni binary alloys with varying ratios in their respective research teams. The alteration of the ratio resulted in changes in the crystal microstructure, ultimately impacting the hydrogen absorption and release capabilities of the alloy [22,23]. The influence of this phenomenon on the thermodynamic properties of the alloy material was further investigated in a subsequent study by Dischinger et al. [24]. In another study, Chesalkin et al. highlighted the specific synthesis parameters of various La-Ni binary compounds through detailed analysis. They also discussed the current status and future significance of the system in the context of energy sources [6]. Among these compounds, $LaNi_5$ is recognized as one of the most promising commercial solid hydrogen storage alloys due to its high hydrogen storage capacity. Many researchers have reported that hydrogen atoms can enter the $LaNi_5$ lattice, occupying tetrahedral or octahedral interstices, to form metal hydrides for hydrogen storage

https://doi.org/10.70322/gct.2025.10014

[8,9,12]. Joubert et al. provided a comprehensive overview of the properties of materials based on $LaNi_5$ and its derivatives, including their electrochemical, thermodynamic, and kinetic properties [1]. These properties play a crucial role in the hydrogen absorption and release capacity of hydrogen storage alloys. Additionally, researchers have shown interest in the electromagnetic properties of $LaNi_5$ alloy. Stucki et al. discussed the electromagnetic properties of $LaNi_5$ and other materials, which positively impacted the electromagnetic applications of this alloy system [7]. Due to its unique superlattice structure, La_2Ni_7 exhibits better hydrogen storage performance than $LaNi_5$. It has also been demonstrated to possess a distinctive low-temperature discharge capacity [25]. Iwase et al. studied the crystal structure changes and phase transitions of La_2Ni_7 during hydrogen absorption using in situ XRD, while Iwatake specifically investigated the crystal structure changes of the two coexisting La_2Ni_7 hydrides formed at hydrogen absorption saturation [26,27]. Additionally, several superconducting materials exist in the La-Ni binary system, such as La_3Ni and La_7Ni_3, as reported in previous studies [13,14]. The La-Ni-Si system comprises various compound proportions, serving purposes in hydrogen storage and superconductivity. Numerous researchers have delved into the composition and performance of this system [2,3,28,29]. Mayer et al. tested the crystallographic data of rare earth silicides at high temperature using in situ XRD and found that binary compounds were generally more stable than ternary compounds, which is reflected in their performance [30]. Baisheva mentioned that in intermetallic compounds, the addition of a small amount of impurities may act as a catalyst and increase the active site [31]. Kakuta et al. explored the hydrogen absorption and discharge characteristics of several La-Na-Si ternary compounds in experiments, while Dakka et al. comprehensively compared $LaNi_5$ with $La_{28.9}Ni_{67.55}Si_{3.55}$. The study showed that after Si replaced Ni, the hydrogen storage would decrease slightly, but the thermodynamic and kinetic performance would greatly improve [32,33]. In the La-Ni-Si system, many superconducting materials have been discovered. Kasahara et al. found that $La_3Ni_4Si_4$ is a superconducting material. Winiarski et al. compared it with $La_3Ni_4Ge_4$, another superconducting material, and found that they were highly similar in many properties, providing direction and ideas for exploring more similar superconducting materials [15,34]. Furthermore, Smetana et al. recently employed single-crystal X-ray diffraction to identify four new compounds in the La-Ni-Si system. They noted the existence of unknown phases that necessitate further investigation [35]. Previous studies have shown that these two systems play an important role in material science and application, but there are few studies on the symbiosis of the two, and the rules of symbiosis have an important impact on the growth and performance of materials.

Single-crystal X-ray diffraction (SXRD) has become a powerful technique for the accurate determination of crystal structures, enabling researchers to gain insight into the arrangement and bonding of atoms in materials [36]. Deriving an unknown and complex crystal structure from powder X-ray diffraction (PXRD) data alone remains a very difficult and even impossible task. However, SXRD measurements can provide not only precise atomic coordinates, bond lengths, and bond angles but also atomic thermal displacements and occupancy rates, which are unavailable from PXRD even when measured using highly monochromatized and very intense synchrotron radiation [37]. By utilizing cutting-edge SXRD techniques, we will demonstrate how high-quality data can be obtained for solving and refining the atomic positions of each phase.

In this paper, we investigated the crystal structure evolution of La-Ni binary alloys under varying oxygen partial pressures using SXRD, EDX, and TEM. Initially, the nominal chemical composition of La_3Ni_2 samples produced via the arc melting method. Then the mixture was coated with a tantalum sheet as well as vacuum sealed, followed by the same high-temperature sintering conditions. The crystal structural information, their topological features, and crystallographic orientation relationships, including their microstructures of those phases during such different synthesized conditions, have been investigated.

2. Materials and Methods

High-purity La (99.99%) blocks and high-purity Ni (99.99%) blocks were weighed according to a molar ratio 3:2, with a total mass of 20 g. Argon (Ar) was used as a protective gas and introduced into a melting furnace. During arc melting, the current was set within the range of 200 A–300 A, and the pressure was maintained at 0.05 MPa. These materials underwent four melting cycles to ensure a uniform composition. After melting, the resulting alloy ingot is crushed into small pieces ranging from tens to hundreds of microns in size. First, a portion of the sample was wrapped in a tantalum sheet, placed in a heat treatment furnace, and maintained at 1100 °C for 5 h before being cooled within the furnace. Second, part of arc melted sample was placed in a quartz tube with a diameter of 6 mm and vacuum-sealed. The sealed glass tube was then subjected to heat treatment in a heat treatment furnace. Among them, the heat treatment conditions for the tantalum-coated and vacuum-sealed samples were identical. The sample was initially heated from

room temperature to 200 ℃ and held for 5 min to remove any residual water, followed by heating to 1100 ℃ and maintained at that temperature for 5 h. The heating rate is consistently set at 10 °C per minute. Afterwards, the temperature of the furnaces equilibrates to room temperature. It needs to be mentioned that the stoichiometry of La_3Ni_2 (metastable according to the La-Ni binary phase diagram as shown in Figure S20 of the supplementary material) was initially selected as a precursor to synthesize the recently reported $La_3Ni_2O_7$ superconducting material [16–18] with the purpose of clarifying its crystallographic features. However, a piece of single crystal with coexistence of three-phase LaNi, $La_3Ni_3Si_2$ and La_2NiSi (see the La-Ni-Si ternary phase diagram as shown in Figure S21 of the supplementary material) was discovered serendipitously as reported in the present work. It needs to be noted that the contamination probably originated from the quartz tube, which was cracked due to the outside pressure (1 atm) of the furnace and inside pressure of the sealed tube during the heat treatment, resulting in a large contact area of the deformed tube with the samples. Consequently, some Si diffuses into the La-Ni sample. Another group has also observed contamination of Si/SiO_2 emitted from the quartz tube [38].

The La-Ni alloy samples obtained through three different treatment methods (through melting, tantalum sheet wrapping, and vacuum-sealed tube) were subsequently tested using SXRD. The diffraction was measured using a four-circle single crystal X-ray diffractometer (Bruker D8 Ventures, Bruker AXS GmbH, Karlsruhe, Germany). In order to verify the accuracy of phase measurement by SXRD, two SEM and EDX tests have been conducted on the vacuum sealed tube sample. In the first test, the electron microscope Hitachi S-3400N type equipped with EDX (EDAX Inc., Mahwah, NJ, USA) at a cathode voltage of 20 kV was used to characterize the morphology and chemical composition. In the second test, the electron microscope ZEISS Sigma 300 type equipped with EDX (Oxford, UK) at a cathode voltage of 15 kV was used to characterize the morphology and chemical composition. SEM and EDX analysis of the single crystal sample can be found in the supplementary material. The results are in good agreement with the phases tested by SXRD. TEM (JEM-F200, JEOL, Tokyo, Japan) equipped with an energy dispersive X-ray spectrometer (EDX) operated at 200 kV. The sample was prepared using the powder dispersion method for the TEM observation. The powder sample dispersed in anhydrous alcohol was sonicated to prepare a suspension, and then part of the suspension was sucked by a rubber dropper and dropped on a copper grid. After drying, a TEM test was performed.

All datasets from SXRD were processed by the APEX3 program [39], including indexing, integration, scaling, absorption correction [40], space group determination [41], structure solving, and refinement [34,42]. Structural models were plotted with the Diamond program (Version 4.6.8) [43]. Building clusters for the studied phases was analyzed by the ToposPro software package (Version 5.5.2.0) [44].

3. Results

3.1. SXRD Test of Synthesized Sample by the Melting Method

The La_3Ni_2 sample obtained through the melting method was analyzed using the SXRD test. The results indicated that both LaNi and La_7Ni_3 phases coexisted within the sample. According to the results of the SXRD test, the sample consists of several La_7Ni_3 and LaNi twins. Figure 1 and Figure 2 show the reciprocal points of the La_7Ni_3 and LaNi twins. Figure 1 presents the reciprocal points of the triple-twinned La_7Ni_3. Figure 1a shows the reciprocal points of the triple-twinned La_7Ni_3 along a random direction. Figure 1b–d sequentially illustrate the reciprocal lattice of the triple-twinned La_7Ni_3 along the c^* axis. The indexed crystal parameters confirm that these are La_7Ni_3 twins. Figure 2 displays the reciprocal points of twinned LaNi. Figure 2a shows the reciprocal points of the LaNi twinning along a random direction. Figure 2b–d sequentially illustrate the reciprocal lattice of the LaNi twinning along the a^* axis. The indexed crystal parameters confirm that these are LaNi twins. This method for confirming twin crystals was also employed in another paper previously published by our group [45]. In Figure 1b, there are 2662 white diffraction points. In Figure 1c, there are 2179 green diffraction points. In Figure 1d, there are 2570 yellow diffraction points. In Figure 2b, there are 1740 red diffraction points. In Figure 2c, there are 622 purple diffraction points. To facilitate the analysis and refinement of the crystal structure, the La_7Ni_3 phase and the LaNi phase, which have the largest number of diffraction points (without intersection with diffraction points from other grains), were selected for crystal structure refinement. The reciprocal lattices of the La_7Ni_3 and LaNi phases projected in three axes and their crystal structures are shown in Figure S1 and Figure S2 of the supplementary material. The reciprocal lattice is a lattice made up of points known as reciprocal points. It is a geometric approach used to describe crystal structures, having a reciprocal relationship with the spatial lattice. Each reciprocal point in the reciprocal lattice corresponds to a set of lattice planes with the same crystal plane spacing in the spatial lattice.

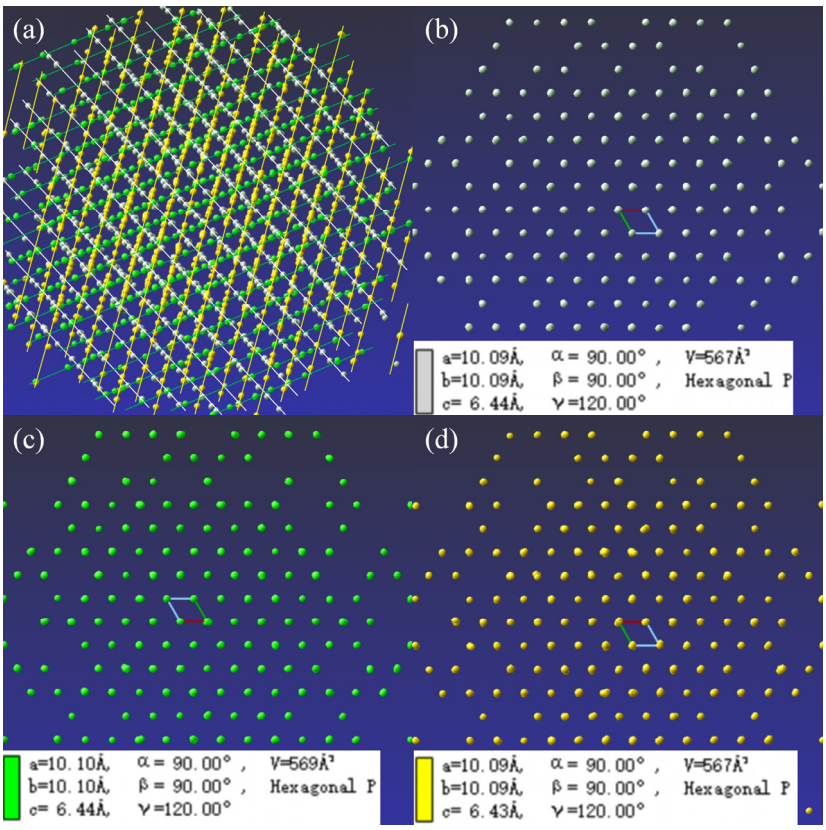

Figure 1. The reciprocal points of the La_7Ni_3 triple twins (**a**), the reciprocal points of the first layer of La_7Ni_3 twins (**b**), the reciprocal points of the second layer of La_7Ni_3 twins (**c**), the reciprocal points of the third layer of La_7Ni_3 twins (**d**).

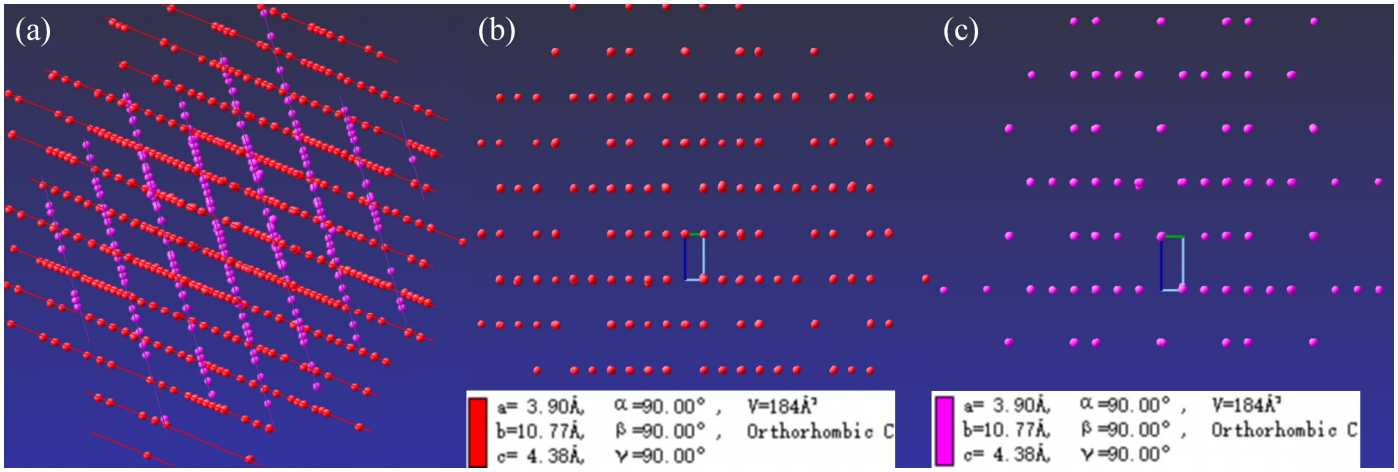

Figure 2. The reciprocal points of LaNi twins (**a**), the reciprocal points of the first layer of LaNi twins (**b**), the reciprocal points of the second layer of LaNi twins (**c**).

Detailed crystallographic data, data collection, and structural refinement details for the La_7Ni_3 and LaNi phases are summarized in Table 1. The crystallographic parameters of both phases adhere to the standards established by international crystallography for the rationalization of crystal structures.

Table 1. Crystallographic and experimental data of La_7Ni_3 and LaNi obtained through arc melting.

	La_7Ni_3	**LaNi**
a/Å	10.0995(18)	3.9014(4)
b/Å	10.0995(18)	10.7782(12)
c/Å	6.4490(16)	4.3854(5)
α, *β*, *γ*/°	90, 90, 120	90, 90, 90
V/Å^3	569.7(2)	184.41(3)
Z	8	2

Space group	$P6_3mc$	$Cmcm$
Crystal system	Hexagonal	Orthorhombic
Diffractometer	Bruker D8 Venture Photon 100 COMS	
Monochromator	Graphite	
T_{meas}/K	300(2)	
Radiation	Mo-Kα, λ = 0.71073 (Å)	
Scan mode	φ and ω scan	
Time per step/s	5	
Absorption correction	Multi-scan	
F(000)	966	340
θ range/°	3.93~27.50	3.78~27.49
μ/mm^{-1}	30.372	32.472
No. measured reflections	4501	2438
No. unique reflections	388	109
No. observed reflections (I > 2σ(I))	337	104
No. reflections used in refinement	388	109
No. parameters used in refinement	22	9
Reflection range	$-12 \le h \le 11$, $-12 \le k \le 11$, $-6 \le l \le 7$	$-4 \le h \le 4$, $-12 \le k \le 12$, $-5 \le l \le 5$
R_{int}	0.1072	0.0657
R(σ)	0.0479	0.0192
Final R indices (Fobs > 4σ(Fobs))	R_1 = 0.0316, ωR_2 = 0.0615	R_1 = 0.0153, ωR_2 = 0.0326
R indices (all data)	R_1 = 0.0359, ωR_2 = 0.0615	R_1 = 0.0165, ωR_2 = 0.0326
Goodness of fit	1.094	1.243

Table 2 presents detailed information on La_7Ni_3, indicating that all atoms are fully occupied at their respective positions. The coordinate positions and occupancy of each atom are highly consistent with Olcese reported in 1973 [46].

Table 2. Fractional atomic coordinates and equivalent isotropic displacement parameters (Å^2) of La_7Ni_3.

Label	Site	*x*	*y*	*z*	Occ.	U_{eq}
La1	2*b*	0.333333	0.666667	0.7870(5)	1	0.0129(7)
La2	6*c*	0.12531(11)	0.87469(11)	0.0006(2)	1	0.0145(5)
La3	6*c*	0.53923(11)	0.46077(11)	0.8123(3)	1	0.0152(5)
Ni1	6*c*	0.8120(2)	0.1880(2)	0.0586(6)	1	0.0173(10)

Next, the building units in the structure of the La_7Ni_3 phase were analyzed using the nanocluster method in Topospro software (Version 5.5.2.0). The nanocluster method can be used to decompose the structure into construction units and describe the overall structural model in the form of combinations. This approach simplifies the structure, making it more intuitive and facilitating the identification of connections and differences between different structures. Through topology analysis, the La_7Ni_3 phase structure can be described by the cluster model of La1(1)(1@15). The cluster is centered on the La1 atom. Figure 3a demonstrates the cluster assembly model of the La_7Ni_3 phase. There are two La1(1)(1@15) clusters in the La_7Ni_3 cell, and the connections between clusters are collinear. Figure 3b depicts the environment diagram of the La1 atom, showing 15 surrounding atoms, including 3 La2 atoms, 9 La3 atoms and 3 Ni1 atoms. In addition, the distances between each coordination atom and the central atom La1 are indicated in Figure 3b. The longest distance, measuring 4.0553 Å, is observed between the La3 and La1 atoms, while the shortest distance, at 2.9382 Å, occurs between the Ni1 and La1 atoms.

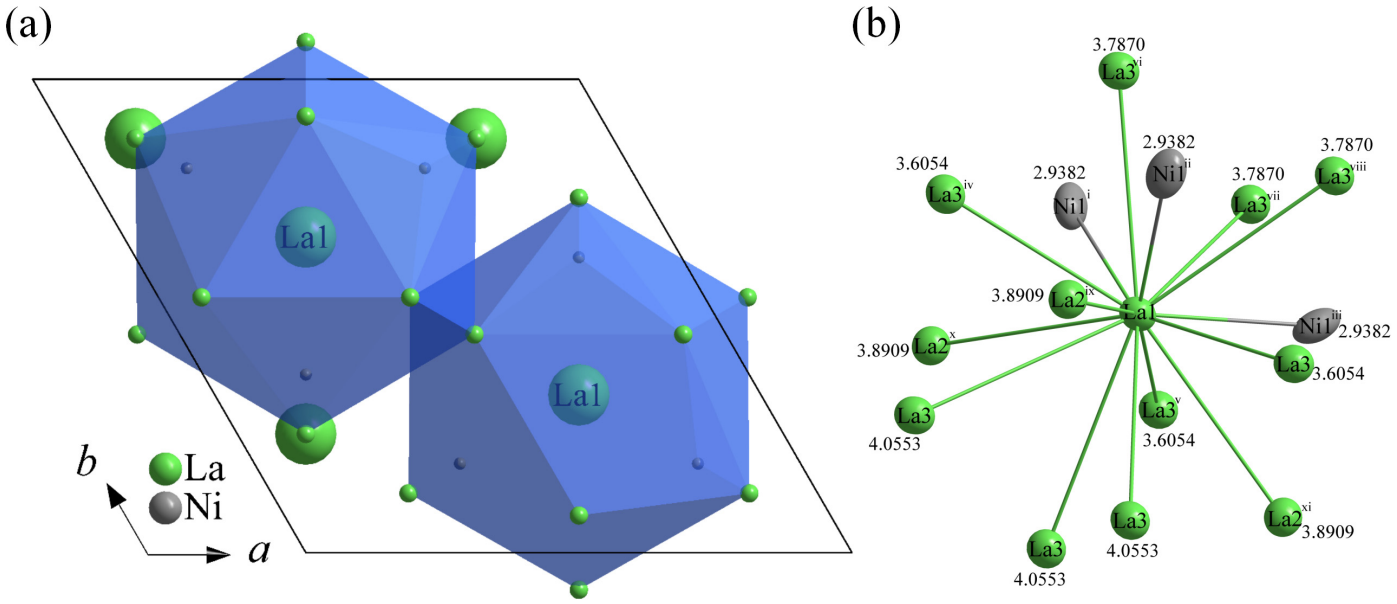

Figure 3. Cluster assembly model of La_7Ni_3 phase (**a**) and atomic environment diagram of La1 atom (**b**). Symmetry codes: (i) $-x + 1, -y + 1, z + 1/2$; (ii) $y, -x + y + 1, z + 1/2$; (iii) $x - y, x, z + 1/2$; (iv) $-y + 1, x-y + 1, z$; (v) $-x + y, -x + 1, z$; (vi) $-x + 1, -y + 1, z - 1/2$; (vii) $x - y, x, z-1/2$; (viii) $y, -x + y + 1, z-1/2$; (ix) $x, y, z + 1$; (x) $-x + y, -x + 1, z + 1$; (xi) $-y + 1, x - y + 1, z + 1$.

Table 3 demonstrates the fractional atomic coordinates, atomic occupancy (Occ.) and equivalent isotropic displacement parameters (U_{eq}) of the LaNi phase. Notably, all atoms have an occupancy of 1. This finding is in strong agreement with the LaNi study by Raman et al. in 1968 [47]. The key distinction is that our study utilizes single crystal X-ray diffraction, whereas the 1968 paper relied on powder X-ray diffraction.

Table 3. Fractional atomic coordinates and equivalent isotropic displacement parameters ($Å^2$) of LaNi.

Label	Site	*x*	*y*	*z*	Occ.	U_{eq}
La1	4*c*	0.000000	0.13715(5)	0.250000	1	0.0116(2)
Ni1	4*c*	0.000000	0.42884(16)	0.250000	1	0.0173(4)

Next, the building units in the structure of the LaNi phase were analyzed using the nanocluster method in Topospro software (Version 5.5.2.0). Through topology analysis, the LaNi phase structure can be described by the cluster model of La1(1)(1@15). The cluster is a octadechedron cluster centered on the La1 atom. Figure 4a illustrates the cluster assembly model of the LaNi phase. There are two La1(1)(1@15) clusters in the LaNi cell, and the connections between clusters are collinear. Figure 4b depicts the environment diagram of the La1 atom, showing 15 surrounding atoms, including 8 La1 atoms and 7 Ni1 atoms. The distances between each coordination atom and the central atom La1 are indicated in Figure 4b. The longest distance, measuring 3.9014 Å, is observed between the La1 and La1 atoms, while the shortest distance, at 2.9743 Å, occurs between the Ni1 and La1 atoms.

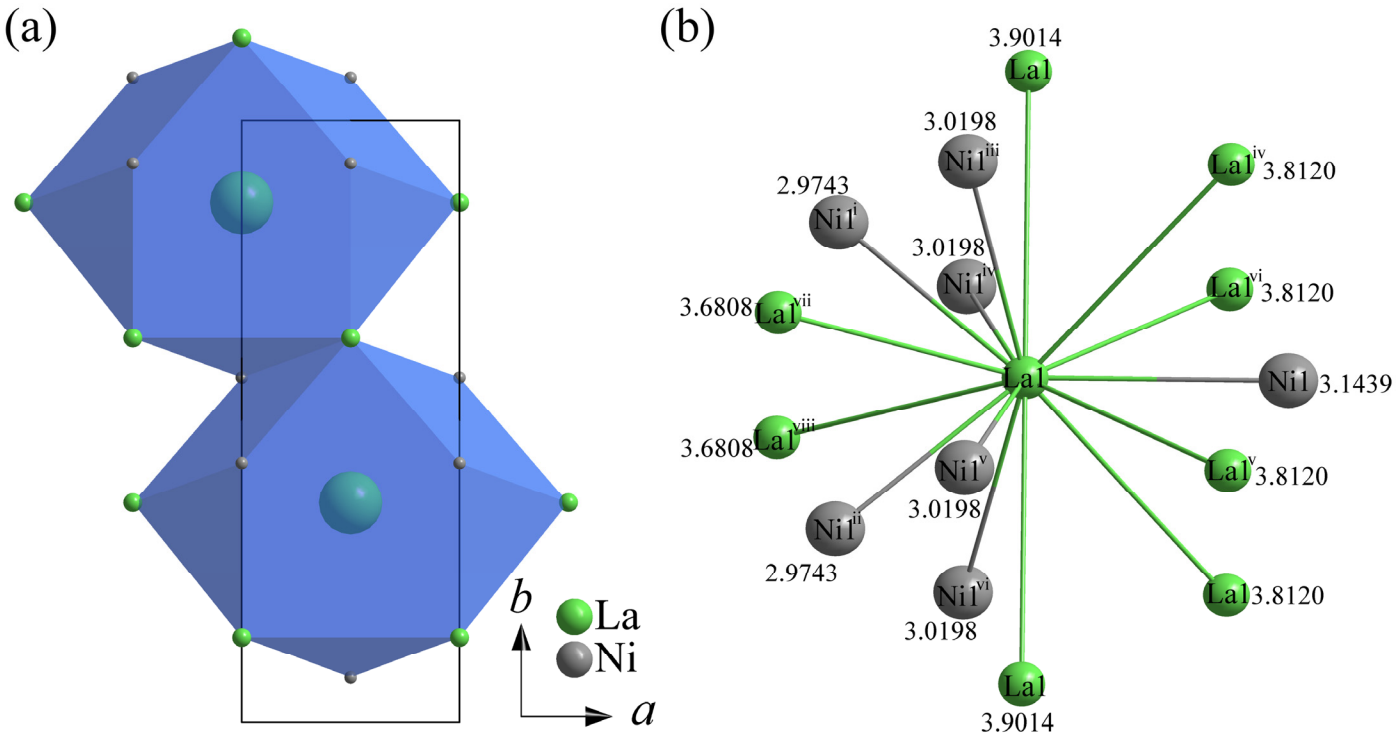

Figure 4. Cluster assembly model of LaNi phase (**a**) and atomic environment diagram of La1 atom (**b**). Symmetry codes: (i) $x - 1/2, y - 1/2, z$; (ii) $x + 1/2, y - 1/2, z$; (iii) $-x - 1/2, -y + 1/2, -z$; (iv) $-x + 1/2, -y + 1/2, -z + 1$; (v) $-x + 1/2, -y + 1/2, -z$; (vi) $-x - 1/2, -y + 1/2, -z + 1$; (vii) $-x, -y, -z$; (viii) $-x, -y, -z + 1$.

3.2. SXRD Test of Tantalum Sheet Wrapped Heat Treatment Sample

Some melted samples were wrapped in tantalum sheets and heat-treated to investigate the structural transformation. Subsequently, SXRD tests were conducted on the samples. The results indicated that the samples were predominantly composed of $LaNi_5$ twins. To facilitate crystal structural refinement, we selected a set of diffraction points exhibiting the strongest diffraction intensity for refinement. The reciprocal lattice and crystal structure of $LaNi_5$ are shown in Figure S3 of the supplementary materials. In addition, an unknown phase is present in this batch of samples. Due to the limited number and weak intensity of the diffraction points associated with this phase, structural refinement cannot be performed. Currently, it is only known that the cell parameter obtained from its indexing are a = 7.23 Å, b = 3.96 Å, c = 6.70 Å, $\alpha = 90°$, $\beta = 94.50°$, $\gamma = 90°$.

Detailed crystallographic data, data collection, and structural refinement details of the $LaNi_5$ phase are summarized in Table 4. The crystallographic parameters of the $LaNi_5$ phase adhere to the standards established by international crystallography for the rationalization of crystal structures.

Table 4. Crystallographic and experimental data of $LaNi_5$ obtained through tantalum sheet-wrapping heat treatment.

	$LaNi_5$
a, b, c/Å	5.0149(4), 5.0149(4), 3.9751(5)
α, β, γ/°	90, 90, 120
V/Å^3	86.577(18)
Z	1
Space group	*P6/mmm*
Crystal system	Hexagonal
Diffractometer	Bruker D8 Venture Photon 100 COMS
Monochromator	Graphite
T_{meas}/K	300(2)
Radiation	Mo-Kα, λ = 0.71073 (Å)
Scan mode	φ and ω scan
Time per step/s	3
Absorption correction	Multi-scan
F(000)	197

θ range/°	4.69~27.47
μ/mm^{-1}	38.406
No. measured reflections	1897
No. unique reflections	47
No. observed reflections (I > 2σ(I))	47
No. reflections used in refinement	47
No. parameters used in refinement	9
Reflection range	$-5 \le h \le 5$, $-5 \le k \le 5$, $-4 \le l \le 4$
R_{int}	0.0670
$R(\sigma)$	0.0181
Final R indices (Fobs > 4σ(Fobs))	R_1 = 0.0294, ωR_2 = 0.0709
R indices (all data)	R_1 = 0.0289, ωR_2 = 0.0709
Goodness of fit	1.374

Table 5 presents detailed information on $LaNi_5$, indicating that La and Ni atoms are fully occupied at their respective positions. The coordinate positions and occupancy of each atom are highly consistent with Thompson et al. reported in 1987 [48].

Table 5. Fractional atomic coordinates and equivalent isotropic displacement parameters (Å^2) of $LaNi_5$.

Label	Site	*x*	*y*	*z*	Occ.	U_{eq}
La1	1*a*	0.000000	0.000000	0.000000	1	0.0061(10)
Ni1	2*c*	0.333333	0.666667	0.000000	1	0.0078(12)
Ni2	3*g*	0.500000	0.000000	0.500000	1	0.0063(11)

Next, the building units in the structure of the $LaNi_5$ phase were analyzed using the nanocluster method in Topospro software (Version 5.5.2.0). Through topology analysis, the $LaNi_5$ phase structure can be described by the cluster model of La1(1)(1@18), which is a icosahedron cluster centered on the La1 atom. Figure 5a illustrates the cluster assembly model of the $LaNi_5$ phase. There are eight La1(1)(1@18) clusters in the $LaNi_5$ cell, and the connections between clusters are coplanar. Figure 5b depicts the environment diagram of the La1 atom, showing 18 surrounding atoms, including 6 Ni1 atoms and 12 Ni2 atoms. In addition, the distances between each coordination atom and the central atom La1 are indicated in Figure 5b. The longest distance, measuring 3.1996 Å, is observed between the La1 and Ni2 atoms, while the shortest distance, at 2.8954 Å, occurs between the Ni1 and La1 atoms.

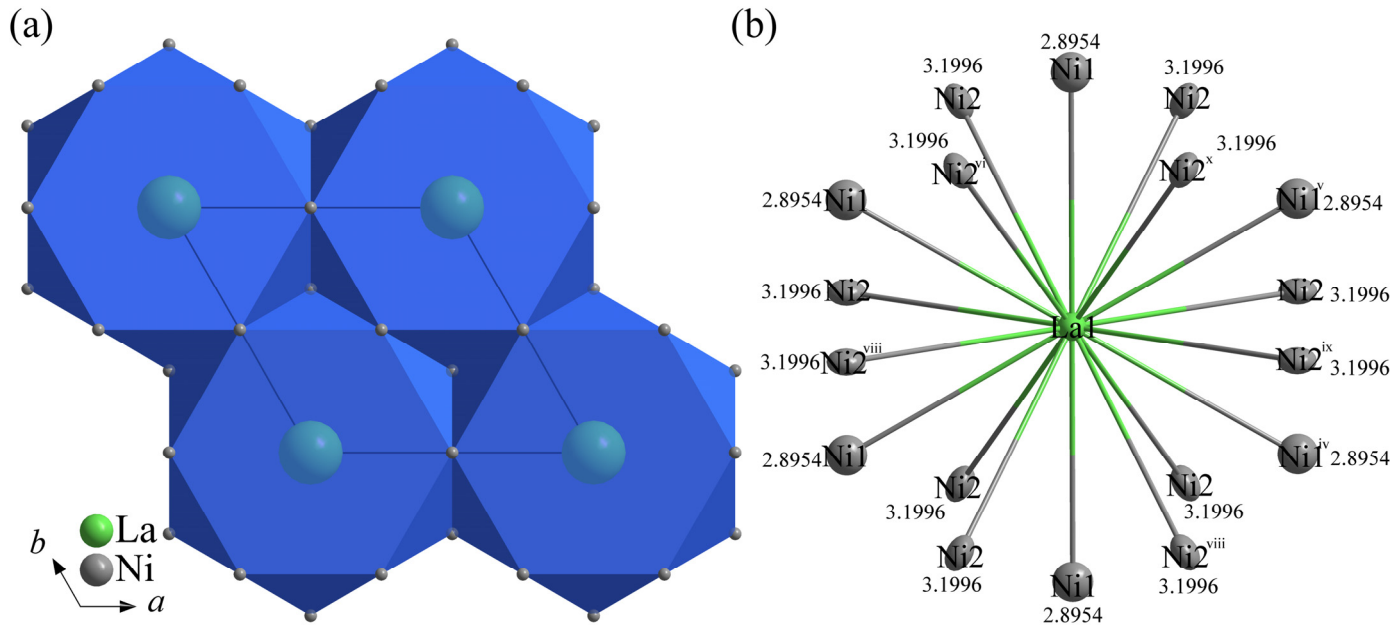

Figure 5. Cluster assembly model of $LaNi_5$ phase (**a**) and atomic environment diagram of La1 atom (**b**). Symmetry codes: (iv) $-x$, $-y+1$, $-z$; (v) x, $y-1$, z; (vi) $-x+y+1$, $-x+1$, z; (viii) $-y$, $x-y$, z; (ix) $x-1$, y, $z-1$; (x) $-y$, $x-y-1$, $z-1$.

3.3. SXRD Test of Vacuum Sealed Tube Samples

In this section, SXRD tests are conducted on samples of vacuum-sealed tube following heat treatment. The diffraction points in the reciprocal space of the collected sample, obtained from the 12 runs of SXRD measurements, are demonstrated in Figure 4. In Figure 6, white spots represent the LaNi phase because the cell parameters after indexing are a = 3.92 Å, b = 10.81 Å, c = 4.39 Å, $\alpha = \beta = \gamma = 90°$. Green spots represent the $La_3Ni_3Si_2$ phase because the cell parameters after indexing are a = 6.11 Å, b = 7.47 Å, c = 14.28 Å, $\alpha = \beta = \gamma = 90°$, and yellow spots represent the La_2NiSi phase because the cell parameters after indexing are $a = b$ = 16.18 Å, c = 4.35 Å, $\alpha = \beta = 90°$, $\gamma = 120°$. It can be clearly divided into three different sets of data sets, which means three independent different phases. Next, the three datasets were analyzed separately. The SXRD analysis of the sample involved a total of 12 runs, resulting in the collection of 8050 diffraction points in reciprocal space when the criterion of I/σ(I) equaled 3 for phase indexing. Within these diffraction points, 2437 were attributed to the LaNi phase, 3131 to the $La_3Ni_3Si_2$ phase, and 1388 to the La_2NiSi phase. The remaining 1094 diffraction points were associated with very small crystalline phases that could not be indexed to determine a unit cell (For a detailed description of the remaining diffraction points, see Figure S5 in Supplementary materials).

The reciprocal lattices of the LaNi, $La_3Ni_3Si_2$ and La_2NiSi phases projected in three axes and their crystal structures are in the Figure S6, Figure S7 and Figure S8 of the supplementary material.

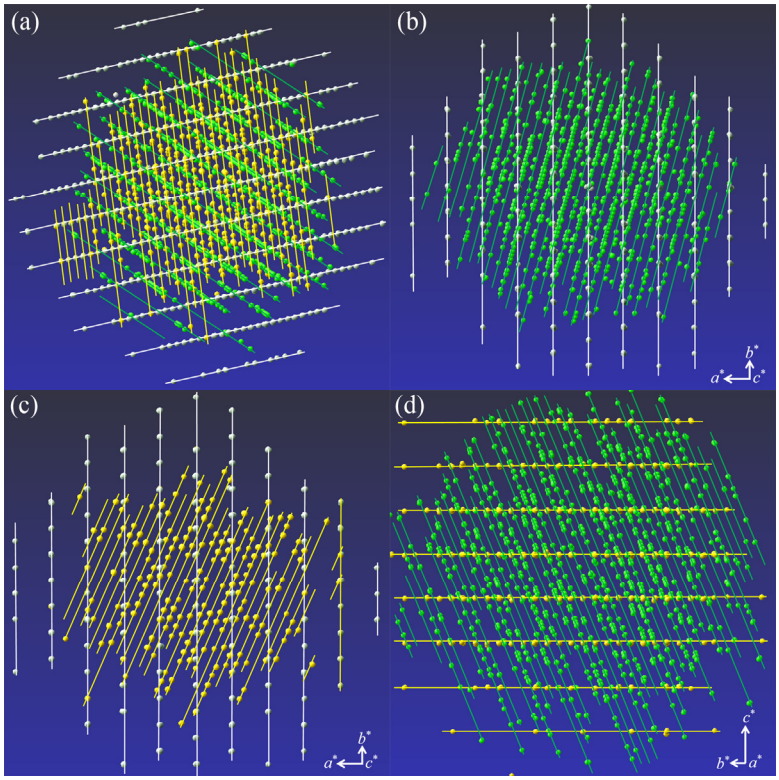

Figure 6. Diffraction spots of the entire sample in the reciprocal space. (**a**) Projection of three sets of data in reciprocal space in a random direction; (**b**) Projection of LaNi phase and $La_3Ni_3Si_2$ phase along the c* axis of LaNi phase; (**c**) Projection of LaNi phase and $La_3Ni_3Si_2$ phase along the c* axis of LaNi phase; (**d**) Projection of $La_3Ni_3Si_2$ phase and La_2NiSi phase along the a* axis of La_2NiSi phase.

Detailed crystallographic data, data collection, and structural refinement details of LaNi phase and $La_3Ni_3Si_2$ phase are summarized in Table 6. The crystallographic parameters of both phases conform to the standards set by international crystallography for the rationalization of crystal structures. For the La_2NiSi phase, due to the limited number of diffraction points and low intensity of the phase, structural refinement is not feasible. However, the crystal structure of La_2NiSi has been previously reported [49,50]. Therefore, the crystal structure of the La_2NiSi phase determined by Bodak et al. [49] is utilized in the topological analysis of the phase. It can be observed from Table 6 that the $La_3Ni_3Si_2$ phase exhibits a narrow range of θ values and higher R_{int}, R_1, and R_2 values. This phenomenon is likely attributed to the presence of the three coexisting phases in the measured crystal, which contributes to the aforementioned issues in the final refinement results of the $La_3Ni_3Si_2$ phase. To address this, selected samples from the same batch for SXRD tests and found a sample belonging to $La_3Ni_3Si_2$ phase, the diffraction quality of this sample is quite good. After indexing

the unit cell, it is found that this set of data shows a small number of $La_3Ni_3Si_2$ twins. Among them, 80.8% of the diffraction points belong to the first domain $La_3Ni_3Si_2$, 16.7% belong to the second domain $La_3Ni_3Si_2$, and 2.5% cannot be indexed, these are crystals that are extremely small in size. Since only a small portion of the diffraction points belong to the second domain $La_3Ni_3Si_2$, we refined the crystal structure of the main 80.8% of the diffraction points. The refinement results were very good, and the crystallographic data from the refined results are presented in Table S3 of the supplementary material, while the fractional coordinates and equivalent isotropic displacement parameters of the atoms are displayed in Table S4 of the supplementary material.

Table 6. Crystallographic and experimental data of LaNi and $La_3Ni_3Si_2$ obtained through vacuum-sealed tube heat treatment.

	LaNi	**$La_3Ni_3Si_2$**
a/Å	3.9213(5)	7.435(5)
b/Å	10.7970(13)	14.227(9)
c/Å	4.3833(6)	6.069(4)
α, *β*, *γ*/°	90, 90, 90	90, 90, 90
V/Å^3	185.58(4)	641.9(7)
Z	2	8
Space group	*Cmcm*	*Pnma*
Crystal system	Orthorhombic	Orthorhombic
Diffractometer	Bruker D8 Venture Photon 100 COMS	
Monochromator	Graphite	
T_{meas}/K	300(2)	
Radiation	Mo-K*α*, *λ* = 0.71073 (Å)	
Scan mode	*φ* and *ω* scan	
Time per step/s	5	
Absorption correction	Multi-scan	
F(000)	340	1132
θ range/°	3.77~27.48	5.46~25.38
μ/mm^{-1}	32.266	28.370
No. measured reflections	3183	6122
No. unique reflections	138	581
No. observed reflections (I > 2σ(I))	130	362
No. reflections used in refinement	138	581
No. parameters used in refinement	9	40
Reflection range	$-5 \le h \le 5$, $-14 \le k \le 14$, $-5 \le l \le 5$	$-8 \le h \le 8$, $-16 \le k \le 16$, $-7 \le l \le 7$
R_{int}	0.0611	0.2268
R(σ)	0.0183	0.1225
Final *R* indices (Fobs > 4σ(Fobs))	$R_1 = 0.0248$, $\omega R_2 = 0.0612$	$R_1 = 0.0543$, $\omega R_2 = 0.1150$
R indices (all data)	$R_1 = 0.0263$, $\omega R_2 = 0.0612$	$R_1 = 0.1159$, $\omega R_2 = 0.1150$
Goodness of fit	1.280	1.048

Since the atomic positions and topology of the LaNi phase have been detailed in Section 3.1, we will not elaborate further here.

Table 7 presents detailed information on $La_3Ni_3Si_2$, indicating that the three types of atoms La, Ni, and Si are fully occupied at their respective positions. Compared with the crystal structure of $La_3Ni_3Si_2$ mentioned by Pani et al. in 2022 [2], the coordinate positions and occupancy of each atom are highly consistent.

Table 7. Fractional atomic coordinates and equivalent isotropic displacement parameters (Å^2) of $La_3Ni_3Si_2$.

Label	**Site**	***x***	***y***	***z***	**Occ.**	**U_{eq}**
La1	8*d*	0.01646(18)	0.60636(9)	0.3610(2)	1	0.0127(4)
La2	4c	0.6169(2)	0.25000	0.3744(4)	1	0.0118(6)
Ni1	8*d*	0.1292(4)	0.4596(2)	0.1013(5)	1	0.0121(8)
Ni2	4*c*	0.2745(6)	0.25000	0.5646(8)	1	0.0167(12)
Si1	8*d*	0.3305(8)	0.4121(4)	0.3630(11)	1	0.0087(15)

Next, the topological structure of the $La_3Ni_3Si_2$ phase is analyzed. It is found that the structure of $La_3Ni_3Si_2$ can be described by the model of a La2(1)(1@17) cluster, which is a centered on the La2 atom. Figure 7a illustrates the cluster assembly model in the $La_3Ni_3Si_2$ unit. There are 4 La2(1)(1@17) clusters that are interleaved with each other connections. Figure 7b presents an environmental diagram of the La2 atom, showing 17 atoms around it, including 6 La1 atoms, 2 La2 atoms, 2 Ni1 atoms, 3 Ni2 atom, and 4 Si1 atoms. In addition, the distances between each coordination atom and the central atom La1 are indicated in Figure 7b. The longest distance, measuring 4.0125 Å, is observed between the La2 and La2 atoms, while the shortest distance, at 2.7952 Å, occurs between the Ni2 and La2 atoms.

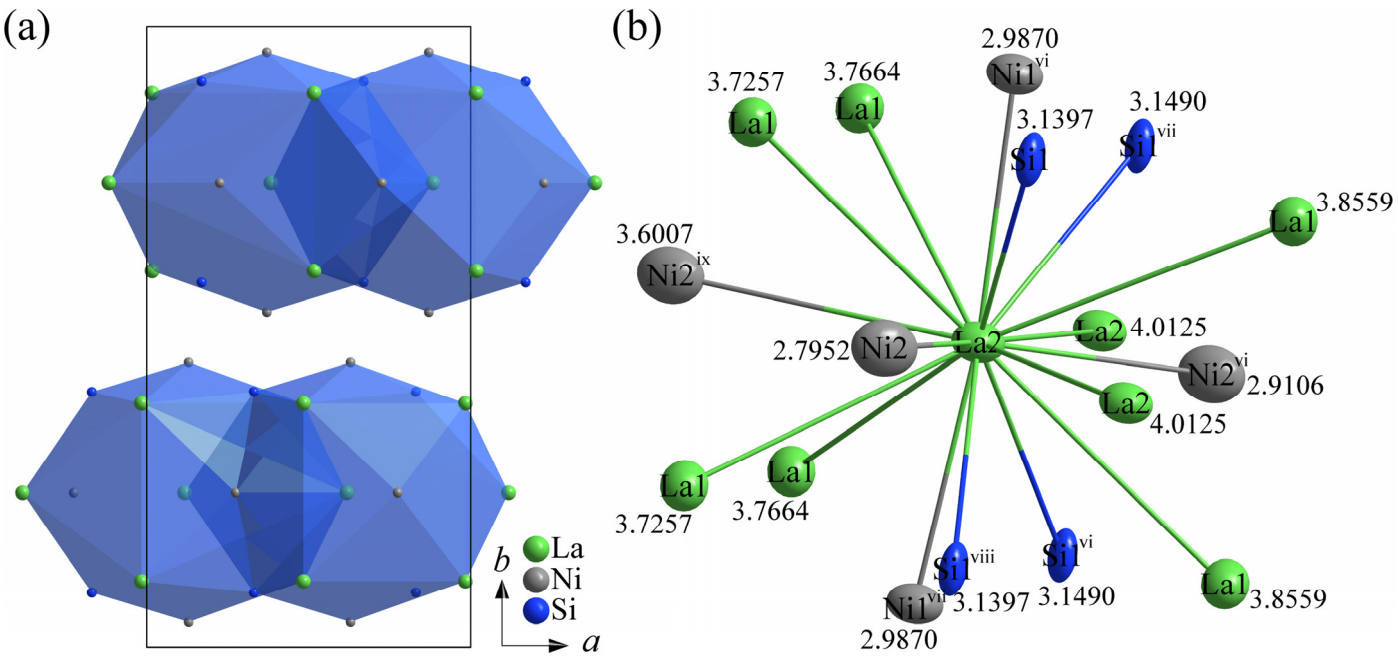

Figure 7. Cluster assembly model of $La_3Ni_3Si_2$ phase (**a**) and atomic environment diagram of La2 atom (**b**). Symmetry codes: (vi) $x + 1/2, y, -z + 1/2$; (vii) $x + 1/2, -y + 1/2, -z + 1/2$; (viii) $x, -y + 1/2, z$; (ix) $x + 1/2, y, -z + 3/2$.

As for the La_2NiSi phase, the structural model of Bodak et al. is used in this paper [49]. Table 8 shows the coordinate positions and occupancy of each atom in the La_2NiSi phase. It can be seen from Table 8 that there are two pairs of co-occupying atoms in the La_2NiSi phase, namely Ni2/Si2 co-occupying atoms and Ni3/Si3 co-occupying atoms.

Table 8. Fractional atomic coordinates of La_2NiSi.

Label	Site	*x*	*y*	*z*	Occ.
La1	6*h*	0.83200	0.82000	0.25000	1
La2	6*h*	0.60200	0.86400	0.25000	1
La3	6*h*	0.38700	0.93300	0.25000	1
La4	2*c*	0.33333	0.66667	0.25000	1
Ni1	2*b*	0.00000	0.00000	0.00000	1
Si1	6*h*	0.54700	0.16700	0.25000	1
Ni2	6*h*	0.75800	0.09200	0.25000	0.45
Si2	6*h*	0.75800	0.09200	0.25000	0.55
Ni3	6*h*	0.71700	0.21900	0.25000	0.90
Si3	6*h*	0.71700	0.21900	0.25000	0.10

Similarly, we conducted a topological analysis of the La_2NiSi phase and found that the phase can be characterized by one cluster model: La2(1)(1@15). The central atom of the La2(1)(1@15) cluster is the La2 atom. Figure 8a illustrates the cluster assembly model in the La_2NiSi phase cell, while Figure 8b depicts the surrounding environment diagram of the La2 atom, which includes 15 atoms: 3 La1 atoms, 4 La3 atoms, 1 La4 atom, 2 Si1 atoms, 3 Si2/Ni2 atoms, and 2 Ni3/Si3 atoms. Additionally, the distances between each coordination atom and the central atom La2 are indicated in Figure 8b. The longest distance, measuring 4.1921 Å, is observed between the La2 and La3 atoms, while the shortest distance, at 3.0406 Å, occurs between the La2 and Ni3/Si3 atoms.

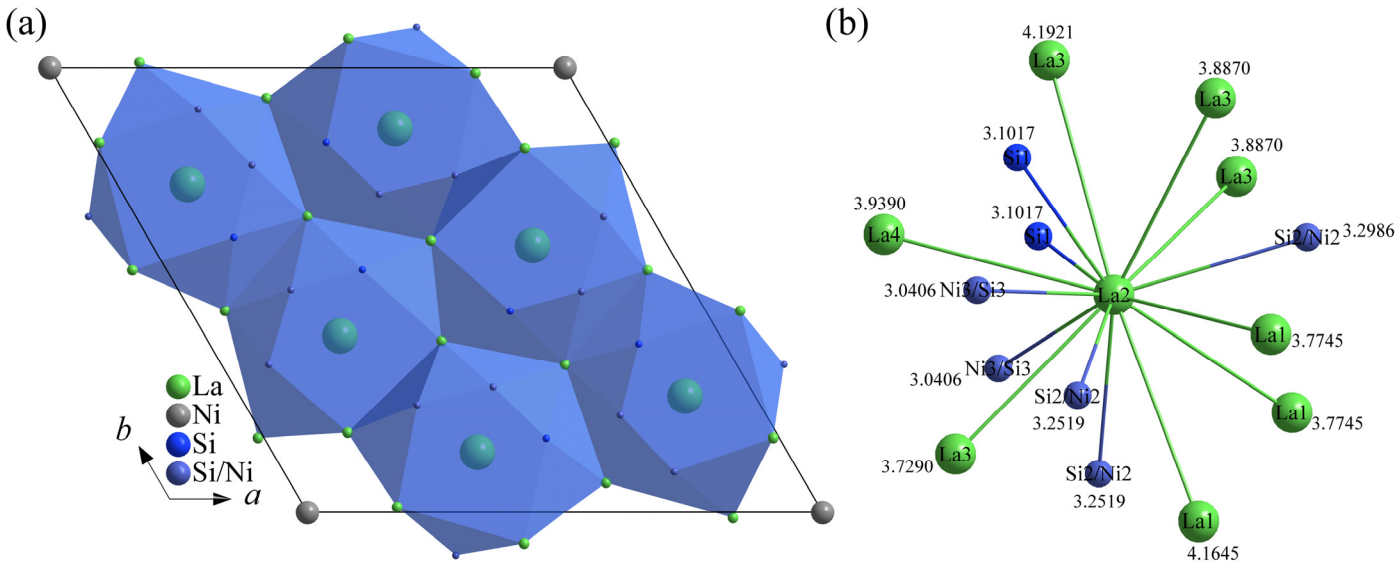

Figure 8. Cluster assembly model of La_2NiSi phase (**a**) and atomic environment diagram of La2 atom (**b**).

3.3.1. TEM Test

In order to verify the accuracy of our SXRD tests, transmission electron microscopy (TEM) analyses were conducted on the same batch of samples. The results are presented in Figures 9–12. Figures 9 and 10 confirm the presence of the La_2NiSi phase, while Figures 11 and 12 confirm the presence of the LaNi phase. It is important to note that although the atomic ratio of La to Ni in Figure 10 is approximately 3:2, the indexing results from the SAED and HRTEM images in Figure 11 are in good agreement with LaNi. Therefore, the sample is considered to be LaNi phase. In addition, only the La_2NiSi and LaNi phases were identified in the TEM test, while the $La_3Ni_3Si_2$ phase was not detected at this time. However, the $La_3Ni_3Si_2$ phase was observed multiple times during the SXRD test. In summary, the TEM test results further confirmed the presence of silicon (Si) elements. Additionally, these findings lend support to the accuracy of our SXRD test results to some extent.

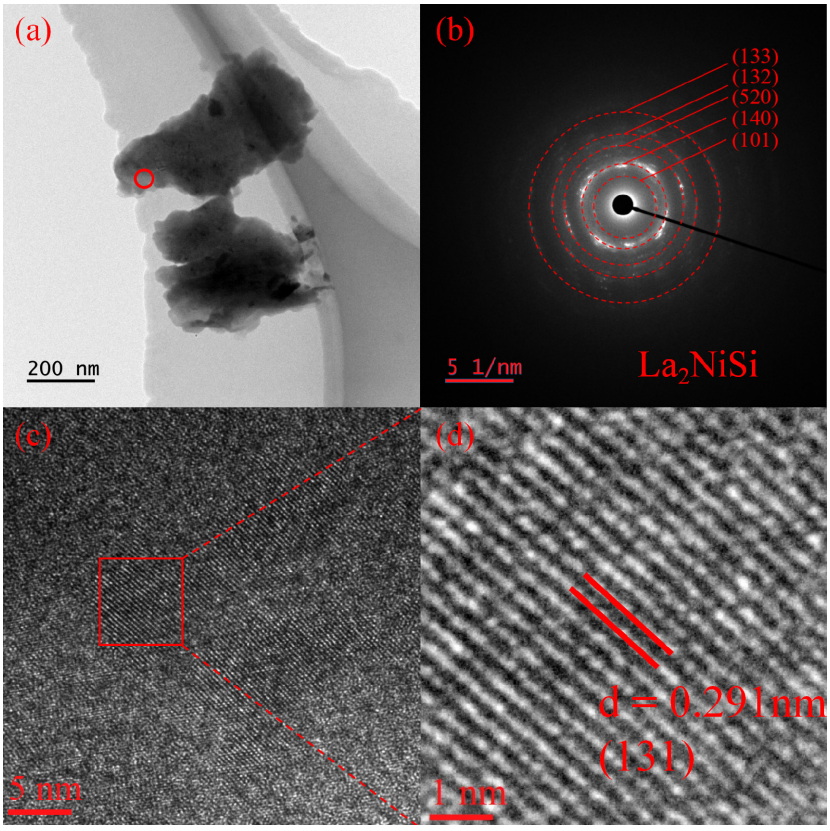

Figure 9. Microstructures of the La_2NiSi phase. (**a**) TEM topography of La_2NiSi phase. (**b**) SAED of La_2NiSi phase. (**c**) HRTEM image for the area outlined by the red circle in (**a**). (**d**) HRTEM image of La_2NiSi acquired from the red box in (**c**).

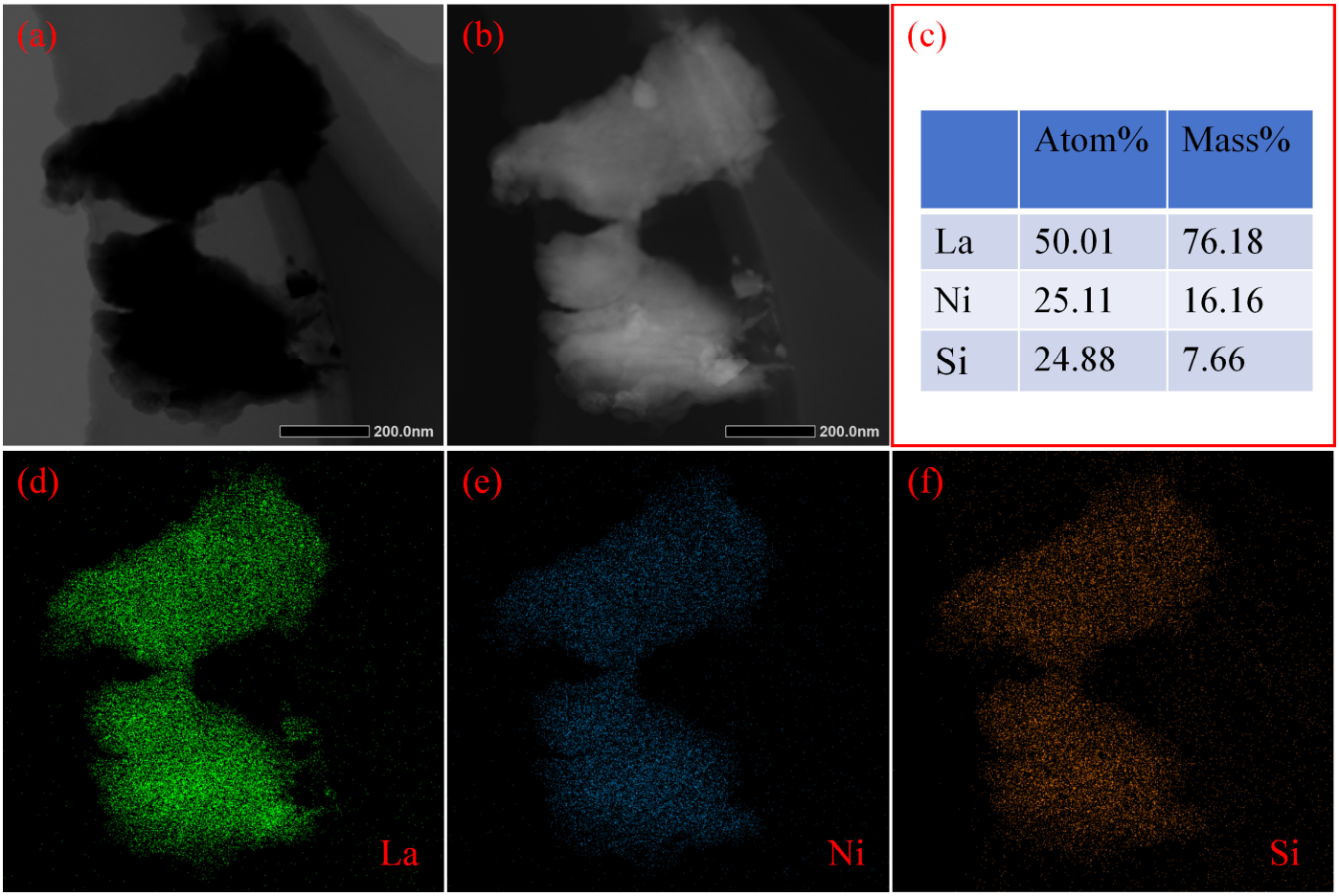

	Atom%	Mass%
La	50.01	76.18
Ni	25.11	16.16
Si	24.88	7.66

Figure 10. STEM image and elemental mappings of La, Ni and Si. (**a**) BF image. (**b**) DF image. (**c**) Element composition test results. (**d**) elemental mapping of La. (**e**) elemental mapping of Ni. (**f**) elemental mapping of Si.

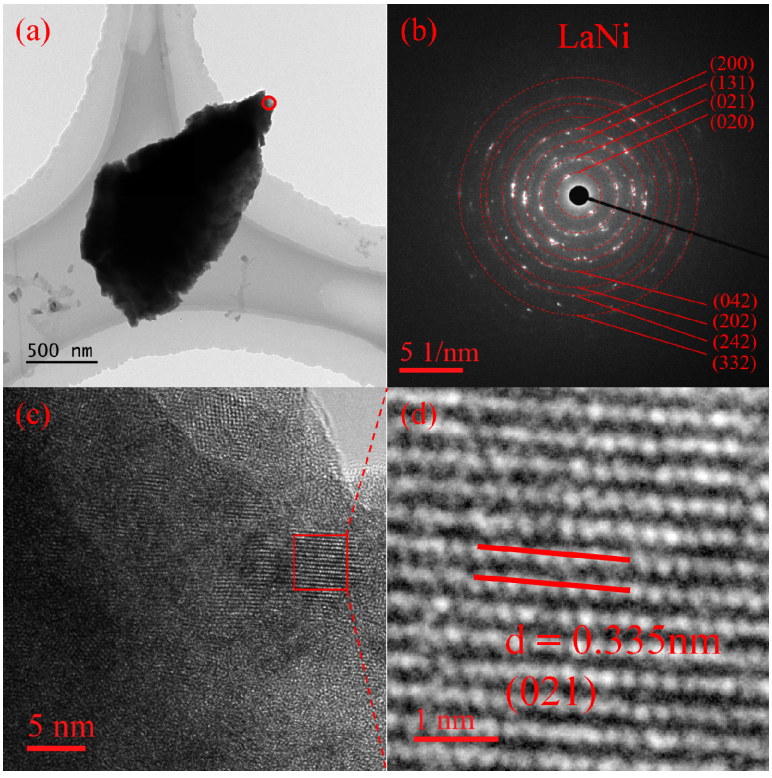

Figure 11. Microstructures of the LaNi phase. (**a**) TEM topography of LaNi phase. (**b**) SAED of LaNi phase. (**c**) HRTEM image for the area outlined by the red circle in (**a**). (**d**) HRTEM image of LaNi acquired from the red box in (**c**).

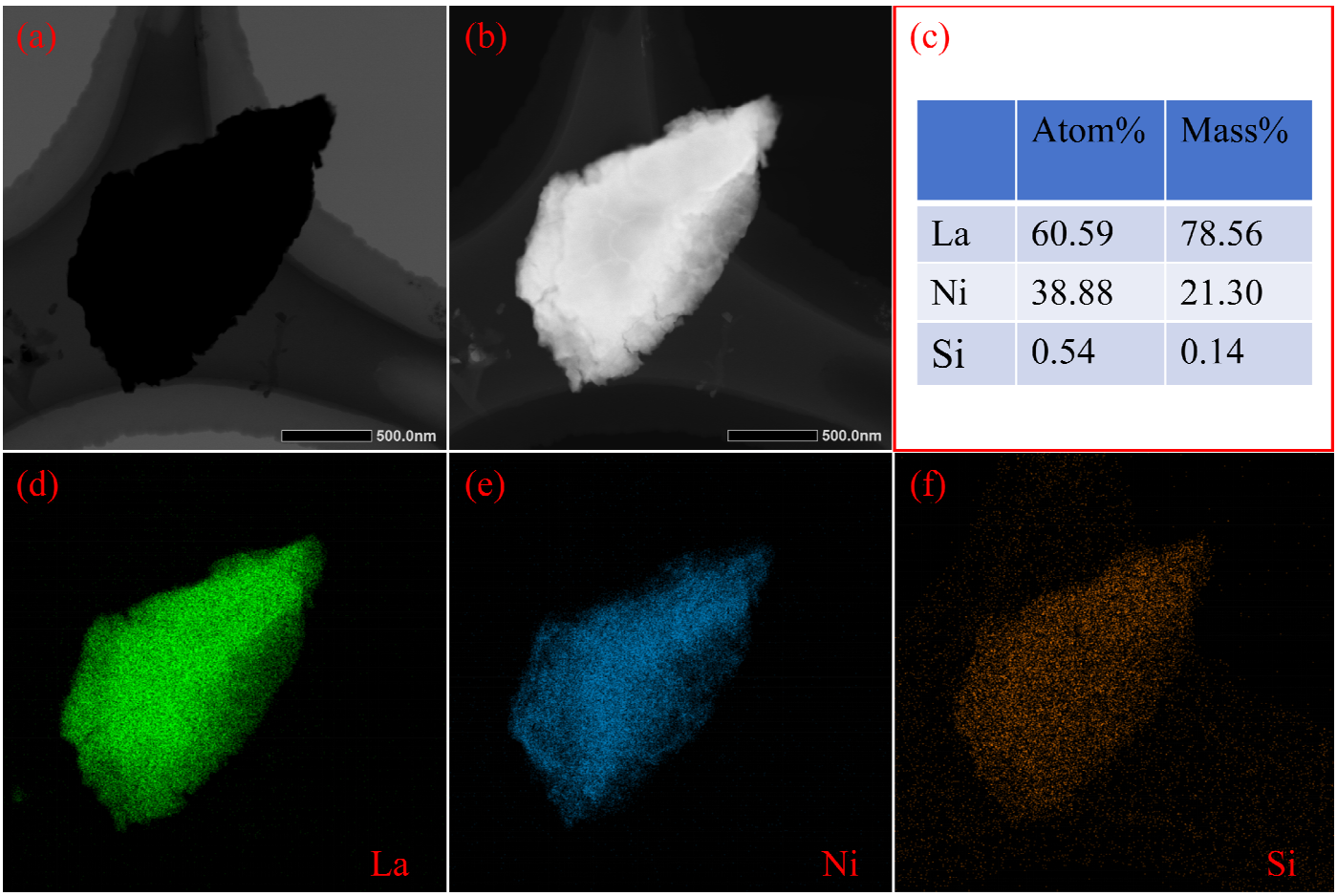

Figure 12. STEM image and elemental mappings of La, Ni and Si. (**a**) BF image. (**b**) DF image. (**c**) Element composition test results. (**d**) elemental mapping of La. (**e**) elemental mapping of Ni. (**f**) elemental mapping of Si.

3.3.2. Construction of Structure Models for Intergrowth LaNi Phase, $La_3Ni_3Si_2$ Phase and La_2NiSi Phase in Real Space

According to the preceding section, it was observed that LaNi, $La_3Ni_3Si_2$, and La_2NiSi are three coexisting phases based on SXRD testing. However, the precise orientation of these three coexisting phases in real space remains unknown. This section aims to establish the orientation model of real space by utilizing the orientation matrices of the LaNi phase, $La_3Ni_3Si_2$, and La_2NiSi phase in reciprocal space. Refer to Appendix A for the detailed method of constructing the orientation model of these three coexisting phases in real space. In a diffraction experiment, the orientation matrix describes the orientation of the single crystal in space. The matrix relates the reciprocal axes of the crystal with the Cartesian coordinate system of the diffractometer. The orientation matrix of the three coexisting phases in reciprocal space is initially determined using APEX3 software. Subsequently, the orientation matrix of the three coexisting phases in real space is derived by establishing the fundamental correspondence between reciprocal space and real space. The orientation model of the interface of the three coexisting phases in real space is then deduced based on the orientation matrix of the three coexisting phases in real space. In Figure 13a, the gray, green, and yellow frames correspond to the LaNi, $La_3Ni_3Si_2$, and La_2NiSi phases, respectively. Finally, the ultimate orientation model depicted in Figure 13b is achieved by introducing atoms to the interface of the three coexisting phase units. Figure 13c illustrates the orientation model of LaNi and $La_3Ni_3Si_2$ phases in real space, while Figure 13d displays the orientation model of LaNi and La_2NiSi phases in real space. Notably, it is evident from Figure 13d that the *c*-axis of the LaNi phase aligns perfectly with that of the La_2NiSi phase.

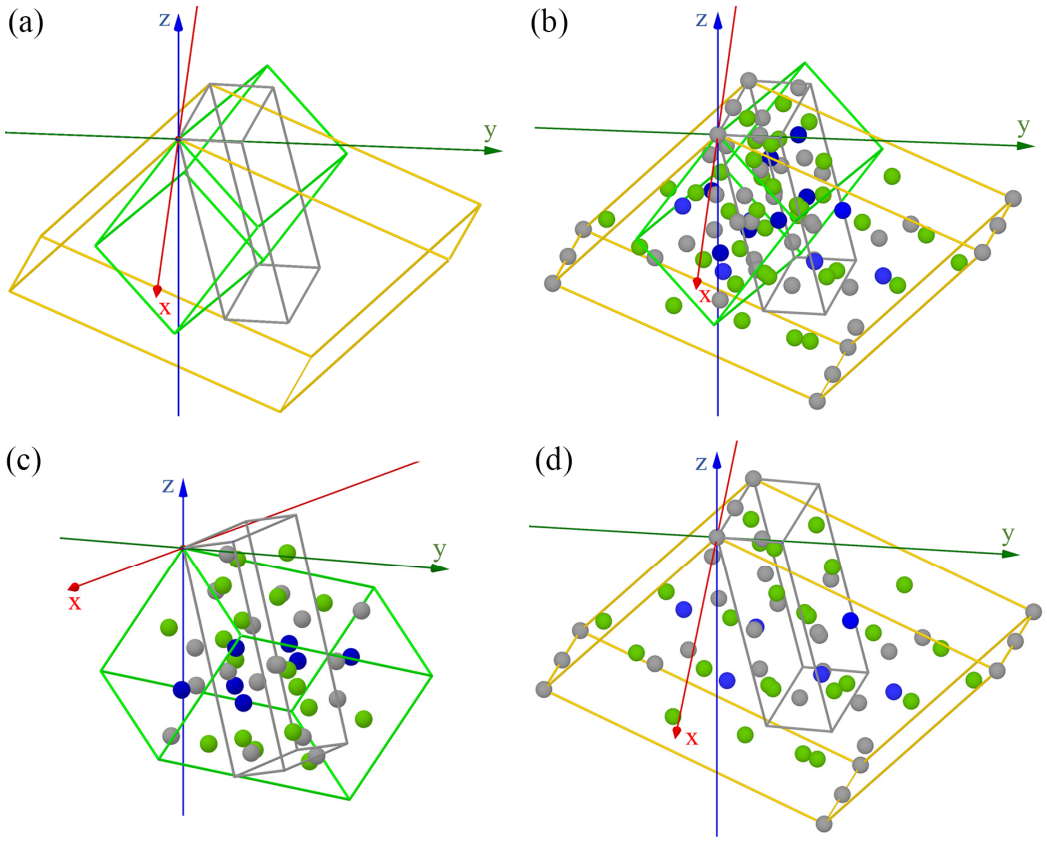

Figure 13. The orientation model of the single-cell border and the LaNi, $La_3Ni_3Si_2$, and La_2NiSi phases after adding atoms in real space is as follows: (**a**) single-cell border, (**b**) LaNi, $La_3Ni_3Si_2$, and La_2NiSi three coexisting phases, (**c**) LaNi and $La_3Ni_3Si_2$ two phases, (**d**) LaNi and La_2NiSi two phases. (The green atoms are La atoms, the gray atoms are Ni atoms, and the blue atoms are Si atoms).

3.3.3. Interface between the LaNi Phase and the $La_3Ni_3Si_2$ Phases

In the previous section, we obtained oriented structural models for the LaNi, $La_3Ni_3Si_2$, and La_2NiSi phases. However, the orientation of the three coexisting phases interface and the arrangement of atoms within the interface remain ambiguous. In this section, we will focus on addressing these issues by studying the synthetic precession images of the SXRD dataset as shown in Figures 14 and 15. Figure 14a, b and c represent the precession images of the (0*kl*), (*h*0*l*) and (*hk*0) planes from the LaNi phase while the Figure 14d, e and f represent the precession images of the (0*kl*), (*h*0*l*) and (*hk*0) planes from the $La_3Ni_3Si_2$ phase. In Figure 14a–c, the precession images are constructed with a thickness of 0.01 $Å^{-1}$ and a resolution of 0.80 Å. While in Figure 14d–f, the precession images are constructed with a thickness of 0.05 $Å^{-1}$ and a resolution of 0.80 Å. In Figure 14, the white and green circles represent the crystal planes of the LaNi and $La_3Ni_3Si_2$ phases, respectively. Figure 14 directly shows the orientation relationship between the LaNi and La3Ni3Si2 phases represented by a pair of crystal planes. These diffraction points from the two phases overlap, mean that they represent crystal planes parallel to each other. In summary, five orientation relationships were obtained from Figure 14a, c, d, e and f, named OR1, OR2, OR3, OR4 and OR5, as shown in Table 9.

Figure 15a, b and c represent precession images of the (0*kl*), (*h*0*l*) and (*hk*0) planes from the $La_3Ni_3Si_2$ phase, while Figure 15d, e and f represent precession images of the (0*kl*), (*h*0*l*) and (*hk*0) planes from the La_2NiSi phase. In Figure 15, the green and yellow circles represent the crystal planes of the $La_3Ni_3Si_2$ and La_2NiSi phases, respectively. The precession image has a thickness of 0.01$Å^{-1}$ and the resolution of 0.80 Å. From Figure 15a, b and f, three orientation relationships between $La_3Ni_3Si_2$ and La_2NiSi phases are obtained, named OR6, OR7 and OR8. These three orientation relationships are shown in Table 10.

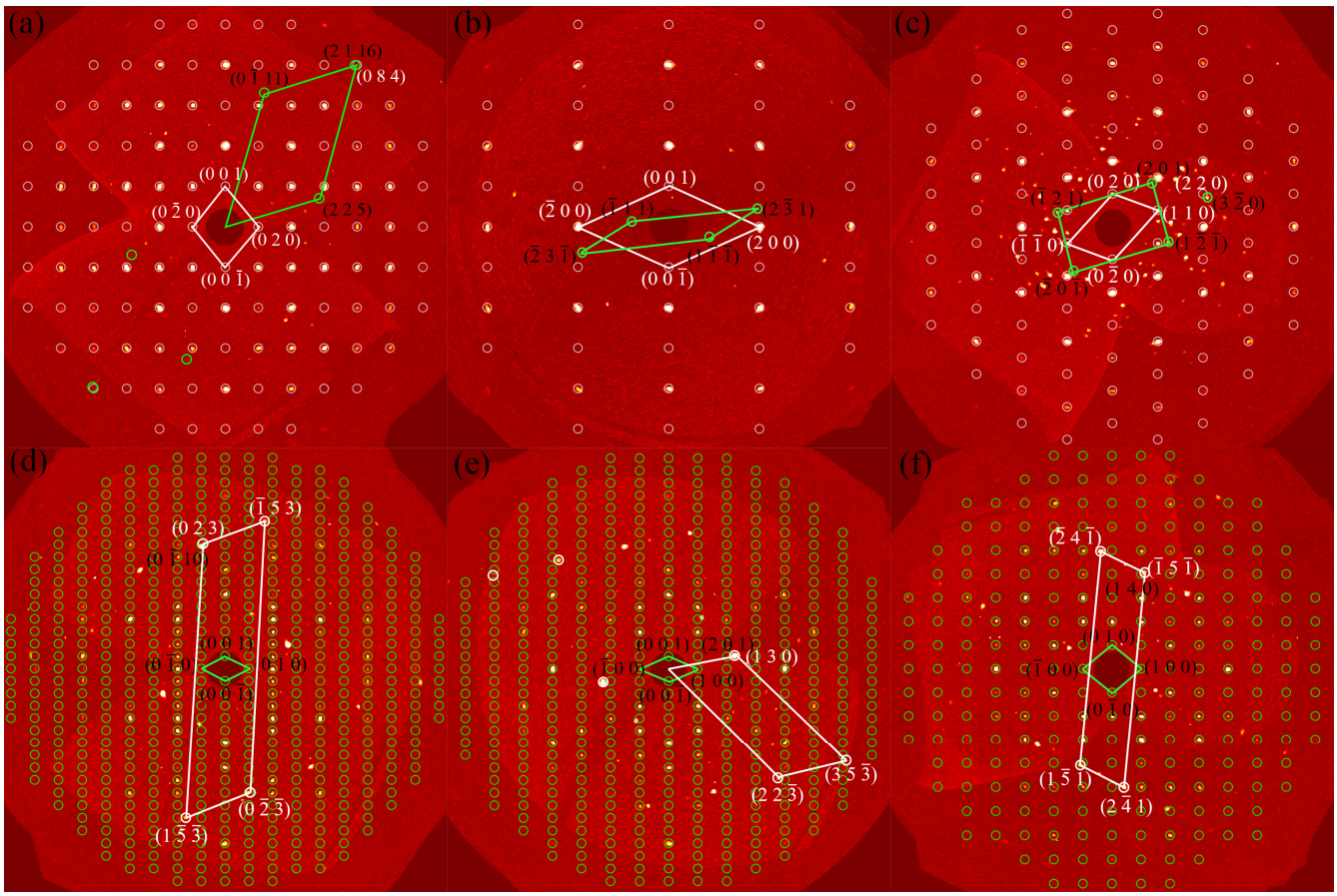

Figure 14. The precession images of intergrowth crystals: (**a**) LaNi (0*kl*), (**b**) LaNi (*h*0*l*), (**c**) LaNi (*hk*0), (**d**) $La_3Ni_3Si_2$ (0*kl*), (**e**) $La_3Ni_3Si_2$ (*h*0*l*), (**f**) $La_3Ni_3Si_2$ (*hk*0).

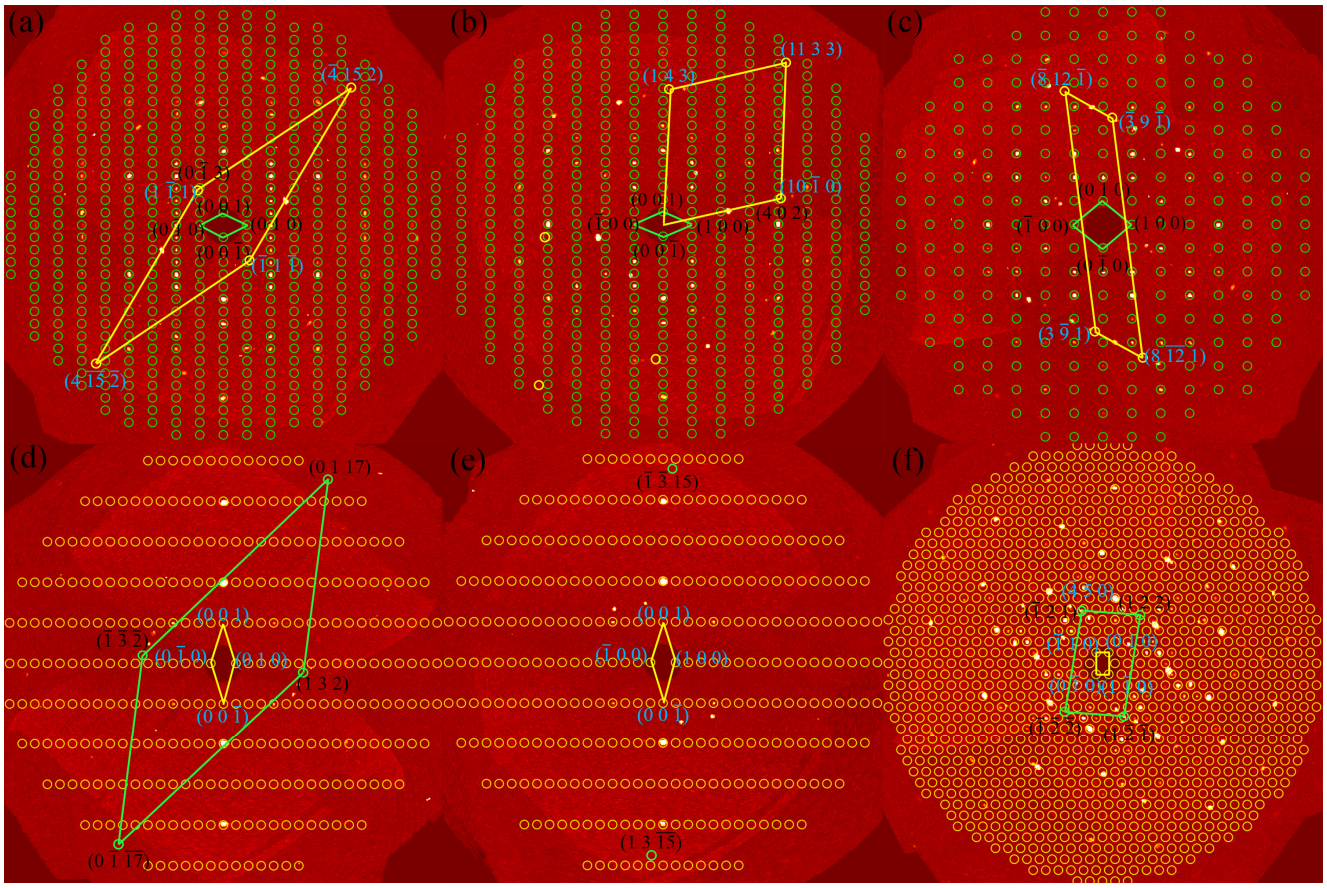

Figure 15. The precession images of intergrowth crystals: (**a**) $La_3Ni_3Si_2$ (0*kl*), (**b**) $La_3Ni_3Si_2$ (*h*0*l*), (**c**) $La_3Ni_3Si_2$ (*hk*0), (**d**) La_2NiSi (0*kl*), (**e**) La_2NiSi (*h*0*l*), (**f**) La_2NiSi (*hk*0).

Table 9. Five crystallographic orientation relationships at the interface of LaNi and $La_3Ni_3Si_2$.

	$[uvw]_{LaNi}//[uvw]_{La3Ni3Si2}$	$(hkl)_{LaNi}//(hkl)_{La3Ni3Si2}$
OR1	$[100]_{LaNi}//[27\bar{2}\bar{2}2]_{La3Ni3Si2}$	$(084)_{LaNi}//(2\ 1\ 16)_{La3Ni3Si2}$
OR2	$[001]_{LaNi}//[23\bar{4}]_{La3Ni3Si2}$	$(220)_{LaNi}//(3\bar{2}0)_{La3Ni3Si2}$
OR3	$[\bar{9}\bar{3}2]_{LaNi}//[100]_{La3Ni3Si2}$	$(023)_{LaNi}//(0\bar{1}10)_{La3Ni3Si2}$
OR4	$[\bar{9}3\bar{4}]_{LaNi}//[010]_{La3Ni3Si2}$	$(130)_{LaNi}//(201)_{La3Ni3Si2}$
OR5	$[\bar{1}16]_{LaNi}//[001]_{La3Ni3Si2}$	$(\bar{1}5\bar{1})_{LaNi}//(140)_{La3Ni3Si2}$

Table 10. Three crystallographic orientation relationships at the interface of $La_3Ni_3Si_2$ and La_2NiSi.

	$[uvw]_{La3Ni3Si2}//[uvw]_{La2NiSi}$	$(hkl)_{La3Ni3Si2}//(hkl)_{La2NiSi}$
OR6	$[100]_{La3Ni3Si2}//[\bar{1}7\bar{6}11]_{La2NiSi}$	$(0\bar{1}3)_{La3Ni3Si2}//(1\bar{1}1)_{La2NiSi}$
OR7	$[010]_{La3Ni3Si2}//[3\ 30\bar{4}\bar{1}]_{La2NiSi}$	$(402)_{La3Ni3Si2}//(10\bar{1}0)_{La2NiSi}$
OR8	$[23\bar{4}]_{La3Ni3Si2}//[001]_{La2NiSi}$	$(\bar{1}21)_{La3Ni3Si2}//(\bar{4}50)_{La2NiSi}$

In order to more intuitively express the five orientation relationships listed in Table 9 and the three orientation relationships listed in Table 10, they are represented by stereoscopic projection diagrams, as shown in Figures 16 and 17.

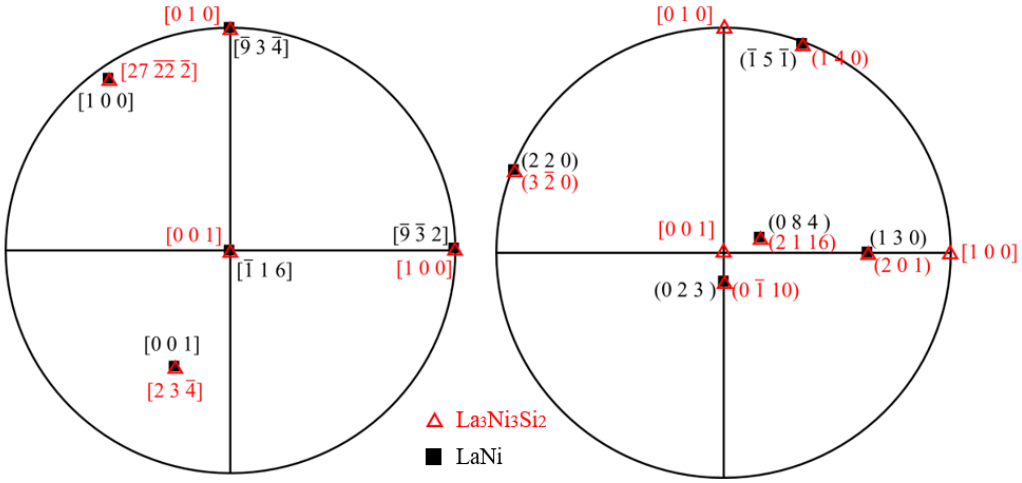

Figure 16. Stereographic projection of the orientation relationships between LaNi and $La_3Ni_3Si_2$ based on the $La_3Ni_3Si_2$ phase: the orientation relationships between crystal directions (**left**), the orientation relationships between crystal planes (**right**).

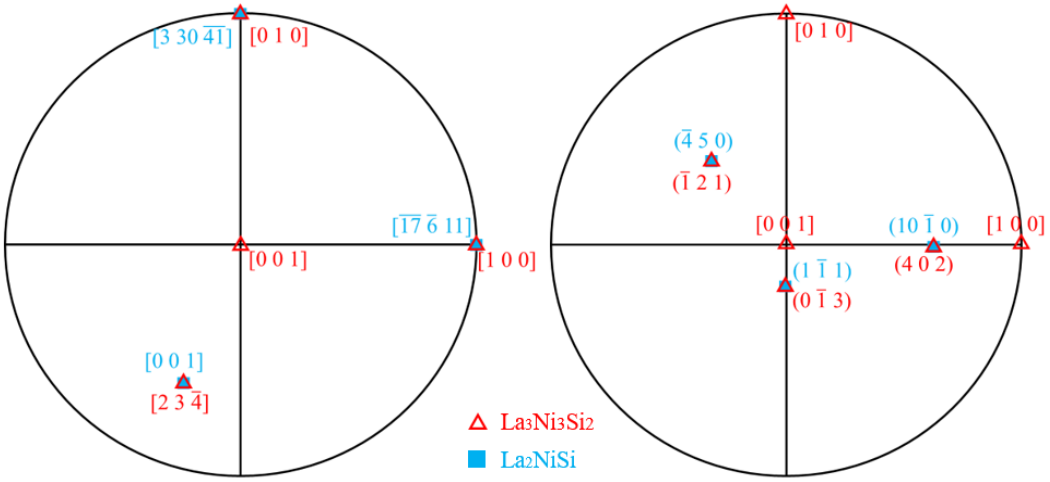

Figure 17. Stereographic projection of the orientation relationships between $La_3Ni_3Si_2$ and La_2NiSi based on the $La_3Ni_3Si_2$ phase: the orientation relationships between crystal directions (**left**), the orientation relationships between crystal planes (**right**).

As mentioned above, Figure 14 identifies five crystal orientation relationships between the LaNi and $La_3Ni_3Si_2$ phases. Three crystal orientation relationships of the $La_3Ni_3Si_2$ phase and La_2NiSi phase can be determined from Figure 15. According to the symmetry principle of crystallography, a set of experimentally determined orientation relationships

often has multiple variants. Therefore, it is necessary to determine whether the eight crystal orientation relationships observed in this experiment are equivalent. Next, we use the matrix method to analyze and discuss the experimental results. The matrix method is used to determine the conversion relationship between the crystal plane index and the crystal direction index between two phases mathematically. This involves finding the transformation matrices B and A for each type of orientation relation. If the absolute values of the nine elements in the transformation matrix are the same, it indicates that the orientation relation of the two phases belongs to the same type, even if the positive/negative signs, arrangement order, and position are different. A detailed description of the matrix approach can be found in our group's previous research [51]. This method obtained the transformation matrix for the eight orientation relations. They are presented in Tables 11 and 12 below. Table 11 shows the conversion matrix for the five crystal orientation relationships between the LaNi and $La_3Ni_3Si_2$ phases, while Table 12 displays the conversion matrix for the three crystal orientation relationships between the $La_3Ni_3Si_2$ and La_2NiSi phases. Where matrix A represents the conversion matrix between crystal planes, and matrix B represents the conversion matrix between crystal directions. It can be determined that there are eight independent orientation relationships because the elements in the transformation matrix corresponding to the eight orientation relationships have different absolute values.

Table 11. Orientation relationships and corresponding conversion matrixes between LaNi and $La_3Ni_3Si_2$ interfaces.

	Orientation Relationship	Conversion Matrix B	Conversion Matrix A
OR1	$(084)_{LaNi}//(2\ 1\ 16)_{La3Ni3Si2}$ $[100]_{LaNi}//[27\ \bar{22}\ \bar{2}]_{La3Ni3Si2}$	$\begin{pmatrix} +1.08 & -1.32 & -0.44 \\ +0.38 & +0.42 & +0.51 \\ -0.27 & -0.60 & +2.96 \end{pmatrix}$	$\begin{pmatrix} +0.45 & -0.37 & -0.03 \\ +1.21 & +0.90 & +0.29 \\ -0.14 & -0.21 & +0.28 \end{pmatrix}$
OR2	$(220)_{LaNi}//(3\bar{2}0)_{La3Ni3Si2}$ $[001]_{LaNi}//[23\bar{4}]_{La3Ni3Si2}$	$\begin{pmatrix} +0.17 & -1.05 & +0.07 \\ +0.19 & -0.22 & -0.07 \\ +0.84 & +1.87 & -9.12 \end{pmatrix}$	$\begin{pmatrix} +1.11 & +0.87 & +0.28 \\ -4.93 & -8.18 & -2.13 \\ +0.05 & +0.07 & -0.09 \end{pmatrix}$
OR3	$(023)_{LaNi}//(0\bar{1}10)_{La3Ni3Si2}$ $[\bar{9}\bar{3}2]_{LaNi}//[100]_{La3Ni3Si2}$	$\begin{pmatrix} -1.37 & +1.90 & +0.69 \\ -0.46 & -0.71 & -0.11 \\ +0.31 & +0.33 & +1.51 \end{pmatrix}$	$\begin{pmatrix} -0.38 & +0.24 & +0.02 \\ -0.97 & -0.84 & +0.38 \\ +0.11 & -0.17 & +0.68 \end{pmatrix}$
OR4	$(130)_{LaNi}//(201)_{La3Ni3Si2}$ $[\bar{9}3\bar{4}]_{LaNi}//[010]_{La3Ni3Si2}$	$\begin{pmatrix} +1.10 & -2.51 & +0.15 \\ +0.43 & +0.84 & +0.35 \\ -0.01 & -1.12 & +1.30 \end{pmatrix}$	$\begin{pmatrix} +0.50 & -0.19 & -0.16 \\ +1.04 & +0.48 & +0.42 \\ -0.33 & -0.11 & +0.68 \end{pmatrix}$
OR5	$(\bar{1}5\bar{1})_{LaNi}//(140)_{La3Ni3Si2}$ $[\bar{1}16]_{LaNi}//[001]_{La3Ni3Si2}$	$\begin{pmatrix} +1.28 & -2.07 & -0.21 \\ +0.55 & +0.84 & +0.21 \\ -0.38 & -1.12 & +1.27 \end{pmatrix}$	$\begin{pmatrix} +0.39 & -0.23 & -0.09 \\ +0.86 & +0.46 & +0.67 \\ -0.08 & -0.12 & +0.66 \end{pmatrix}$

Table 12. Orientation relationships and corresponding conversion matrixes between $La_3Ni_3Si_2$ and La_2NiSi interfaces

	Orientation Relationship	Conversion Matrix B	Conversion Matrix A
OR6	$(0\bar{1}3)_{La3Ni3Si2}//(1\bar{1}1)_{La2NiSi}$ $[100]_{La3Ni3Si2}//[\bar{17}\ \bar{6}\ 11]_{La2NiSi}$	$\begin{pmatrix} -2.02 & +0.36 & +0.11 \\ +0.14 & -1.76 & -0.74 \\ +0.73 & -1.27 & +0.44 \end{pmatrix}$	$\begin{pmatrix} -0.51 & -0.18 & +0.33 \\ -0.09 & -0.29 & -0.68 \\ +0.02 & -0.44 & +1.03 \end{pmatrix}$
OR7	$(402)_{La3Ni3Si2}//(10\bar{1}0)_{La2NiSi}$ $[010]_{La3Ni3Si2}//[3\ 30\ \bar{41}]_{La2NiSi}$	$\begin{pmatrix} +2.43 & -0.68 & -0.32 \\ -0.45 & +1.07 & -0.11 \\ -0.18 & +0.89 & +0.64 \end{pmatrix}$	$\begin{pmatrix} +0.44 & +0.17 & -0.12 \\ +0.09 & +0.85 & -1.17 \\ +0.24 & +0.24 & +1.30 \end{pmatrix}$
OR8	$(\bar{1}21)_{La3Ni3Si2}//(\bar{4}50)_{La2NiSi}$ $[23\bar{4}]_{La3Ni3Si2}//[001]_{La2NiSi}$	$\begin{pmatrix} -0.78 & -1.82 & +0.30 \\ -1.75 & +1.04 & +0.45 \\ -0.43 & -0.05 & -0.60 \end{pmatrix}$	$\begin{pmatrix} -0.22 & -0.43 & +0.13 \\ -0.38 & +0.21 & +0.29 \\ -0.39 & -0.06 & -1.40 \end{pmatrix}$

Furthermore, a preliminary interface model of these interface relationships was established. Take OR1 orientation relationship: $[001]_{LaNi}//[23\bar{4}]_{La3Ni3Si2}$, $(220)_{LaNi}//(3\bar{2}0)_{La3Ni3Si2}$ as an example. For the $(220)_{LaNi}$ surface model, as shown in Figure 18a, the *u* and *v* directions are parallel to [001] and $[1\bar{1}0]$, respectively. At this time, the lattice parameters on the surface of $(020)_{LaNi}$ are: u = 4.383 Å, v = 11.487 Å, and θ = 90°. For the surface model of $(3\bar{2}0)_{La3Ni3Si2}$, as shown in Figure 18b, the *u* and *v* directions are parallel to $[23\bar{4}]$ and [2 3 13], respectively. The lattice parameters on the surface of $(3\bar{2}0)_{La3Ni3Si2}$ are as follows: u = 51.304 Å, v = 90.926 Å, θ = 88.43°. Considering the significant mismatch between the surfaces of (220) LaNi and $(3\bar{2}0)$ $La_3Ni_3Si_2$, it is essential to construct a supercell interface model to minimize the disparity. It was observed that utilizing the 12(u) × 8(v) (220) LaNi interface and the 1(u) × 1(v) $La_3Ni_3Si_2$ interface led to relatively minor mismatches, with $\delta(u)$ = 2.52% and $\delta(v)$ = 1.07% discrepancies in the *u* and *v* directions, respectively. Figure 18c displays the atomic interface model of LaNi(220)/ $La_3Ni_3Si_2(3\bar{2}0)$.

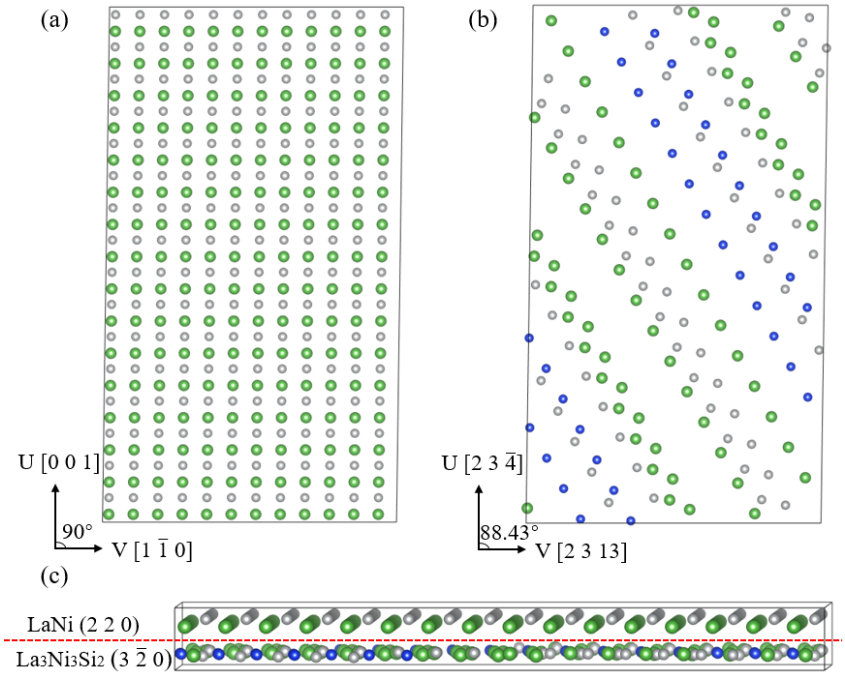

Figure 18. (**a**): (220) surface of the LaNi phase; (**b**): (3$\bar{2}$0) surface of the $La_3Ni_3Si_2$ phase; (**c**): the atomic interface model of LaNi(220)/ $La_3Ni_3Si_2$(3$\bar{2}$0) (The green atoms are La atoms, the gray atoms are Ni atoms, and the blue atoms are Si atoms).

4. Summary

We conducted SXRD tests on La-Ni alloys obtained through three different treatment methods in this experiment. Firstly, the La_3Ni_2 samples produced by the melting method consist of La_7Ni_3 and LaNi phases. The space group corresponding to La_7Ni_3 is $P6_3mc$, with the following cell parameters: $a = b = 10.0995(18)$ Å, $c = 6.4490(16)$ Å, $\alpha = \beta = 90°$, $\gamma = 120°$. Topological analysis demonstrates that the La_7Ni_3 phase consists of La1(1)(1@15) type clusters, with the La1 atom serving as the central atom. The corresponding space group for LaNi is *Cmcm*, and its cell parameters are as follows: $a = 3.9014(4)$ Å, $b = 10.7782(12)$ Å, $c = 4.3854(5)$ Å, $\alpha = \beta = \gamma = 90°$. Topological analysis demonstrates that the LaNi phase consists of La1(1)(1@15) type clusters, with the La1 atom serving as the central atom.

Secondly, the phase composition of the La_3Ni_2 sample, after coating with a tantalum sheet and subsequent heat treatment, primarily consists of the $LaNi_5$ phase. The corresponding space group is *P6/mmm*, and the cell parameters are as follows: $a = b = 5.0149(12)$ Å, $c = 3.9751(5)$ Å, $\alpha = \beta = 90°$, $\gamma = 120°$. The crystal structure can be described as composed of La1(1)(1@18) type clusters, with the La1 atom serving as the central atom.

Finally, the phase composition of the La_3Ni_2 sample after vacuum-sealed tube heat treatment consists of LaNi, $La_3Ni_3Si_2$, and La_2NiSi phases, which coexist in three distinct phases. Among these, the space group corresponding to LaNi is *Cmcm*, with the following cell parameters: $a = 3.9213(5)$ Å, $b = 10.7970(13)$ Å, $c = 4.3833(6)$ Å, $\alpha = \beta = \gamma = 90°$. The corresponding space group for $La_3Ni_3Si_2$ is *Pnma*, with cell parameters of $a = 7.435(5)$ Å, $b = 14.227(13)$ Å, $c = 6.069(6)$ Å, $\alpha = \beta = \gamma = 90°$. The crystal structure can be described as composed of La2(1)(1@17) type clusters, with the La2 atom at the center. Due to the limited and weak number of diffraction points, the crystal structure of the La_2NiSi phase cannot be refined. However, the cell parameters of the La_2NiSi phase, after indexing, are known to be $a = b = 16.18$ Å, $c = 4.35$ Å, $\alpha = \beta = 90°$, and $\gamma = 120°$. Furthermore, the synthetic precession images of the SXRD data set were studied to obtain the orientation relationship of the three coexisting phases interface. By analyzing the (0*kl*), (*h*0*l*), and (*hk*0) planes of the three coexisting phases, eight independent orientation relationships were obtained for OR1, OR2, OR3, OR4, OR5, OR6, OR7, and OR8, respectively. Taking OR2 as an example, the preliminary interface model illustrates the arrangement of atoms within the interface.

This study analyzed the phase composition of La-Ni alloys under various treatment methods, which plays an important role in the future study of the La-Ni and La-Ni-Si systems.

Supplementary Materials

The following supporting information can be found at: https://www.sciepublish.com/article/pii/658, Figure S1: Reciprocal lattice patterns of the La_7Ni_3 phase projected in three axes: (a) *a** axis; (b) *b** axis; (c) *c** axis and its crystal structure projected in *c* axis (d); Figure S2: Reciprocal lattice patterns of the LaNi phase projected in three axes: (a) *a** axis; (b) *b** axis; (c) *c** axis, and its crystal structure projected in *c* axis (d); Figure S3: Reciprocal lattice patterns of the $LaNi_5$ phase projected in three axes: (a) *a** axis; (b) *b** axis; (c) *c** axis, and its crystal structure projected in *c* axis (d); Figure S4: (a) The Phi360 diffraction pattern collected in the process of single crystal testing, (b) the powder diffraction pattern obtained by integrating the Phi360 diffraction pattern; Figure S5: Powder diffraction pattern of the remaining 1094 diffraction points (margin). Figure S6: Reciprocal lattice patterns of the LaNi phase projected in three axes: (a) *a** axis; (b) *b** axis; (c) *c** axis, and its crystal structure projected in *c* axis (d); Figure S7: Reciprocal lattice patterns of the $La_3Ni_3Si_2$ phase projected in three axes: (a) *a** axis; (b) *b** axis; (c) *c** axis, and its crystal structure projected in *c* axis (d); Figure S8: Reciprocal lattice patterns of the La_2NiSi phase projected in three axes: (a) *a** axis; (b) *b** axis; (c) *c** axis, and its crystal structure projected in *c* axis (d); Figure S9: The precession images (a) (0*kl*), (b) (*h*0*l*), (c) (*hk*0) crystal planes of LaNi phase in the SXRD test, LaNi phase simulated diffraction pattern with axes in (d) [100], (e) [010], and (f) [001]; Figure S10: The precession images (a) (0*kl*), (b) (*h*0*l*), (c) (*hk*0) crystal planes of $La_3Ni_3Si_2$ phase in the SXRD test, $La_3Ni_3Si_2$ phase simulated diffraction pattern with axes in (d) [100], (e) [010], and (f) [001]; Figure S11: The precession images (a) (0*kl*), (b) (*h*0*l*), (c) (*hk*0) crystal planes of La_2NiSi phase in the SXRD test, La_2NiSi phase simulated diffraction pattern with axes in (d) [100], (e) [010], and (f) [001]; Figure S12: Scanning electron microscope (SEM) micrographs of a single crystal sample. EDX analysis was performed for various locations as indicated in Table S1; Table S1: The EDX results conducted at every scanning location in Figure S12; Figure S13: Scanning electron microscope (SEM) micrographs of single crystal sample. EDX analysis was performed for various locations as indicated in Table S2; Table S2: The EDX results conducted at every scanning location in Figure S13; Figure S14: The precession images: (a) LaNi (1*kl*), (b) LaNi (*h*1*l*), (c) LaNi (*hk*1), (d) $La_3Ni_3Si_2$ (1*kl*), (e) $La_3Ni_3Si_2$ (*h*1*l*), (f) $La_3Ni_3Si_2$ (*hk*1); Figure S15: The precession images: (a) LaNi (2*kl*), (b) LaNi (*h*2*l*), (c) LaNi (*hk*2), (d) $La_3Ni_3Si_2$ (2*kl*), (e) $La_3Ni_3Si_2$ (*h*2*l*), (f) $La_3Ni_3Si_2$ (*hk*2); Figure S16: The precession images: (a) LaNi (3*kl*), (b) LaNi (*h*3*l*), (c) LaNi (*hk*3), (d) $La_3Ni_3Si_2$ (3*kl*), (e) $La_3Ni_3Si_2$ (*h*3*l*), (f) $La_3Ni_3Si_2$ (*hk*3); Figure S17: The precession images: (a) $La_3Ni_3Si_2$ (1*kl*), (b) $La_3Ni_3Si_2$ (*h*1*l*), (c) $La_3Ni_3Si_2$ (*hk*1), (d) La_2NiSi (1*kl*), (e) La_2NiSi (*h*1*l*), (f) La_2NiSi (*hk*1); Figure S18: The precession images: (a) $La_3Ni_3Si_2$ (2*kl*), (b) $La_3Ni_3Si_2$ (*h*2*l*), (c) $La_3Ni_3Si_2$ (*hk*2), (d) La_2NiSi (2*kl*), (e) La_2NiSi (*h*2*l*), (f) La_2NiSi (*hk*2); Figure S19: The precession images: (a) $La_3Ni_3Si_2$ (3*kl*), (b) $La_3Ni_3Si_2$ (*h*3*l*), (c) $La_3Ni_3Si_2$ (*hk*3), (d) La_2NiSi (3*kl*), (e) La_2NiSi (*h*3*l*), (f) La_2NiSi (*hk*3); Figure S20: (a)La-Ni binary convex hull, (b) La-Ni binary phase diagram; Figure S21: La-Ni-Si ternary phase diagram; Table S3: Crystallographic and experimental data of $La_3Ni_3Si_2$ phase in another sample; Table S4: Fractional atomic coordinates and equivalent isotropic displacement parameters ($Å^2$) of $La_3Ni_3Si_2$ phase in another sample.

Appendix A

During data processing, the orientation matrix is a 3 × 3 matrix, which specifies the component values and orientations of the three reciprocal axes based on the *x*, *y*, and *z* coordinates on the goniometer. This matrix therefore contains the basic data that defines the reciprocal cell and its spatial orientation. The orientation matrix in reciprocal space can be described as:

$$\mathrm{R} = \begin{pmatrix} a_x^* & b_x^* & c_x^* \\ a_y^* & b_y^* & c_y^* \\ a_z^* & b_z^* & c_z^* \end{pmatrix} \tag{A1}$$

a^* corresponds to the first column, b^* to the second, c^* to the third. The subscripts *x*, *y*, and *z* indicate the Cartesian coordinates of the diffractometer.

The orientation matrix of LaNi, $La_3Ni_3Si_2$ and La_2NiSi phases in the reciprocal space was recorded using APEX3 software, where the orientation matrix of LaNi phase in the reciprocal space is:

$$\begin{pmatrix} +0.08751311 & -0.00740845 & -0.21358819 \\ +0.23488939 & +0.02130833 & +0.07239119 \\ +0.04850991 & -0.08981182 & +0.03479378 \end{pmatrix} \tag{A2}$$

The orientation matrix of $La_3Ni_3Si_2$ phase in reciprocal space is:

$$\begin{pmatrix} +0.06037243 & +0.00620812 & -0.06503084 \\ +0.12217132 & -0.08172383 & +0.01862565 \\ -0.09075078 & -0.10588900 & -0.01818771 \end{pmatrix} \quad \text{(A3)}$$

The orientation matrix of La_2NiSi phase in reciprocal space is:

$$\begin{pmatrix} +0.01006662 & -0.01470755 & -0.21359995 \\ +0.05206853 & -0.01050337 & +0.07254676 \\ -0.04672600 & -0.06833122 & +0.03482372 \end{pmatrix} \quad \text{(A4)}$$

From the basic correspondence between reciprocal space and real space:

$$a^* \cdot a = b^* \cdot b = c^* \cdot c = 1 \quad \text{(A5)}$$

One can derive the orientation matrix of these two phases in real space. Where the orientation matrix of LaNi phase in real space is:

$$\begin{pmatrix} +1.34253892 & +3.60343910 & +0.74419088 \\ -0.86394990 & +2.48490911 & -10.4735680 \\ -4.10186403 & +1.39023996 & +0.66819876 \end{pmatrix} \quad \text{(A6)}$$

The orientation matrix of $La_3Ni_3Si_2$ phase in real space is:

$$\begin{pmatrix} +2.25216729 & +4.55754897 & -3.38541900 \\ +0.34624554 & -4.55798760 & -5.90575284 \\ -13.25342951 & +3.79594931 & -3.70669660 \end{pmatrix} \quad \text{(A7)}$$

The orientation matrix of La_2NiSi phase in real space is:

$$\begin{pmatrix} +4.64935674 & +15.29827923 & -3.35226173 \\ -5.26866880 & -9.751584356 & -12.00163398 \\ -4.09975509 & +1.39243421 & +0.66839289 \end{pmatrix} \quad \text{(A8)}$$

Through the orientation matrix of LaNi, $La_3Ni_3Si_2$ and La_2NiSi phases in real space, the comprehensive models of LaNi, $La_3Ni_3Si_2$ and La_2NiSi described with cell edges in real space can be constructed. As shown in Figure 17a of the main text.

Now we can add the specific atoms for both phases to the orientation models described with cell edges by acknowledging the experimental orientation matrix and the Crystallographic Information File (CIF) related orientation matrix. Firstly, the positions of the atoms of the LaNi phase in real space are introduced. We named the experimental orientation matrix of the phase in the real space as matrix B. The CIF-related orientation matrix corresponding to the LaNi is described as:

$$A = \begin{pmatrix} 3.9213 & 0 & 0 \\ 0 & 10.7970 & 0 \\ 0 & 0 & 4.3833 \end{pmatrix} \quad \text{(A9)}$$

Based on matrix A and matrix B, one can find the transformation relationship between the two matrices, let AC = B, then the matrix C is:

$$C = \begin{pmatrix} +0.34235872 & +0.91891647 & +0.18977683 \\ -0.08002272 & +0.23016517 & -0.97011617 \\ -0.93585766 & +0.31718914 & +0.15245238 \end{pmatrix} \quad \text{(A10)}$$

Then the cartesian coordinates of the atoms in the CIF of LaNi are multiplied by the matrix C, resulting the coordinate positions of the atoms of the LaNi phase in real space. Secondly, the coordinate positions of the atoms of the $La_3Ni_3Si_2$ phase and La_2NiSi phase in real space are also obtained in the same way. Finally, the comprehensive oriented structural models of LaNi, $La_3Ni_3Si_2$ and La_2NiSi phases in real space are obtained, Figure 17b, 17c and 17d in the main text are the projection of the orientation matrix in a, b and c after filling the atoms, respectively.

Acknowledgments

The authors express gratitude to the Fund of National Natural Science Foundation of China (grant No. 52173231; grant No. 51925105), Hebei Natural Science Foundation (grant No. E2022203182; grant No. E2020203158), Project of Hebei Provincial Department of Human Resources and Social Security (grant No. E2020100006), The Innovation

Ability Promotion Project of Hebei supported by Hebei Key Lab for Optimizing Metal Product Technology and Performance (grant No. 22567609H) for providing financial support for this study.

Author Contributions

Conceptualization, C.F., B.W. and L.Z.; methodology, Y.L. and C.F.; investigation, Y.L., T.R., Z.X. and Y.W., C.F.; writing—original draft preparation, Y.L. and T.R.; writing—review and editing, Z.X., Y.W., C.F., B.W. and L.Z.; supervision, C.F., B.W. and L.Z.; funding acquisition, C.F., B.W. and Z.X. All authors have read and agreed to the published version of the manuscript.

Ethics Statement

Not applicable.

Informed Consent Statement

Not applicable.

Data Availability Statement

Data will be made available on request.

Funding

This research was funded by National Natural Science Foundation of China (grant No. 52173231; grant No. 51925105), Hebei Natural Science Foundation (grant No. E2022203182; grant No. E2020203158), Project of Hebei Provincial Department of Human Resources and Social Security (grant No. E2020100006), and The Innovation Ability Promotion Project of Hebei supported by Hebei Key Lab for Optimizing Metal Product Technology and Performance (grant No. 22567609H).

Declaration of Competing Interest

The authors declare that they have no known competing financial interests or personal relationships that could have appeared to influence the work reported in this paper.

References

1. Joubert JM, Paul-Boncour V, Cuevas F, Zhang J, Latroche M. $LaNi_5$ related AB_5 compounds: Structure, properties and applications. *J. Alloys Compd*. **2021**, *862*, 158163.
2. Pani M, Provino A, Smetana V, Shtender V, Bernini C, Mudring AV, et al. Four ternary silicides in the La–Ni–Si system: From polyanionic layers to frameworks. *CrystEngComm* **2022**, *24*, 8219–8228.
3. Grilli D, Smetana V, Ahmed SJ, Shtender V, Pani M, Manfrinetti P, et al. La n (n+ 1)+ x Ni n (n+ 5)+ y Si (n+ 1)(n+ 2)–z: A Symmetric Mirror Homologous Series in the La–Ni–Si System. *Inorg. Chem.* **2023**, *62*, 10736–10742.
4. Grigorchenko V, Molokeev M, Yurev IO, Aleksandrovsky AS, Oreshonkov AS, Krylov AS, et al. Properties of La2F4Se, B-Lafse Phases. Phase Diagram of the LaF3-La2Se3 System. Phase Diagram of the LaF3-La2Se3 System. *J. Solid State Chem.* **2024**, *338*, 124880.
5. Zagorac D, Buyer C, Zagorac J, Škundrić T, Schön JC, Schleid T. Band-Gap Engineering and Unusual Behavior of Electronic Properties during Anion Substitution of Sulfur in LaFSe. *Cryst. Growth Des.* **2024**, *24*, 1648–1657.
6. Chesalkin A, Moldrik P, Martaus A. La-Ni Based Alloys Preparation for Hydrogen Reversible Sorption and their Application for Renewable Energy Storage. 2018. Available online: https://www.preprints.org/frontend/manuscript/de680b38063f2896adcc4b1fcb4e0262/download_pub (accessed on 1st September 2025).
7. Stucki F, Schlapbach L. Magnetic properties of LaNi5, FeTi, Mg2Ni and their hydrides. *J. Less Common Met.* **1980**, *74*, 143–151.
8. Sato T, Saitoh H, Utsumi R, Ito J, Nakahira Y, Obana K, et al. Hydrogen Absorption Reactions of Hydrogen Storage Alloy $LaNi_5$ under High Pressure. *Molecules* **2023**, *28*, 1256.
9. Zhu W, Yang H, Xu J, Yue S, Wang L, Liu J, et al. Function mechanism of Fe in improving cycle stability and plateau characteristics of AB5-type hydrogen storage alloys. *Int. J. Hydrogen Energy* **2024**, *63*, 1013–1024.

10. Sawahara K, Yatagai K, Boll T, Pundt A, Gemma R. Role of atomic hydrogen supply on the onset of CO_2 methanation over La–Ni based hydrogen storage alloys studied by in-situ approach. *Int. J. Hydrogen Energy* **2022**, *47*, 19051–19061.
11. Zayani W, Dabaki Y, Khaldi C, Lamloumi J, El-Kedim O, Fenineche N. Electrochemical study of the $LaNiO_3$ perovskite-type oxide used as anode in nickel-metal hydride batteries. *Solid State Sci.* **2023**, *146*, 107338.
12. Adarmouch M, Kassaoui ME, Jmal SA, Mounkachi O, Balli M. Unravelling LaNi5 intrinsic degradation: New insights from DFT study on thermodynamics and hydrogen diffusion. *J. Energy Storage* **2024**, *83*, 110664.
13. Sato N, Imamura K, Sakon T, Komatsubara T, Umehara I, Sato K. Is La3Ni a new unconventional superconductor? *J. Phys. Soc. Jpn.* **1994**, *63*, 2061–2065.
14. Nakamura A, Honda F, Homma Y, Li D, Nishimura K, Kakihana M, et al. Single Crystal Growth and Superconductivity in La7Ni3 without Inversion Symmetry in the Crystal Structure. *J. Phys. Conf. Ser*. **2017**, *807*, 052012. IOP Publishing.
15. Kasahara S, Fujii H, Mochiku T, Takeya H, Hirata K. Specific heat of novel ternary superconductors $La_3Ni_4X_4$ (X= Si and Ge). *Phys. C* **2008**, *468*, 1231–1233.
16. Sun H, Huo M, Hu X, Li J, Liu Z, Han Y, et al. Signatures of superconductivity near 80 K in a nickelate under high pressure. *Nature* **2023**, *621*, 493–498.
17. Wang L, Li Y, Xie SY, Liu F, Sun H, Huang C, et al. Structure Responsible for the Superconducting State in $La_3Ni_2O_7$ at High-Pressure and Low-Temperature Conditions. *J. Am. Chem. Soc.* **2024**, *146*, 7506–7514.
18. Wang G, Wang NN, Shen XL, Hou J, Ma L, Shi LF, et al. Pressure-Induced Superconductivity in Polycrystalline $La_3Ni_2O_{7-\delta}$. *Phys. Rev. X* **2024**, *14*, 011040.
19. Chen Z, Yang H, Mebs S, Dau H, Driess M, Wang Z, et al. Reviving oxygen evolution electrocatalysis of bulk La–Ni intermetallics via gaseous hydrogen engineering. *Adv. Mater.* **2023**, *35*, 2208337.
20. Zhou M, Wang Z, Mei A, Yang Z, Chen W, Ou S, et al. Photocatalytic CO_2 reduction using La-Ni bimetallic sites within a covalent organic framework. *Nat. Commun.* **2023**, *14*, 2473.
21. Hojo H, Inohara Y, Ichitsubo R, Einaga H. Catalytic properties of $LaNiO_3$ and Mn-modified $LaNiO_3$ catalysts for oxidation of CO and benzene. *Catal. Today* **2023**, *410*, 127–134.
22. Buschow KH, Van Mal HH. Phase relations and hydrogen absorption in the lanthanum-nickel system. *J. Less Common Met.* **1972**, *29*, 203–210.
23. Yamamoto T, Inui H, Yamaguchi M, Sato K, Fujitani S, Yonezu I, et al. Microstructures and hydrogen absorption/desorption properties of LaNi alloys in the composition range of La77. 8∼83.2 at.% Ni. *Acta Mater*. **1997**, *45*, 5213–5221.
24. Dischinger J, Schaller HJ. On the constitution and thermodynamics of Ni–La alloys. *J. Alloys Compd*. **2000**, *312*, 201–210.
25. Shi S, Ouyang C, Lei M. Crystal structure and electrochemical characteristics of non-AB5 type La–Ni system alloys. *J. Power Sources* **2007**, *164*, 911–915.
26. Iwase K, Sakaki K, Nakamura Y, Akiba E. Phase transformation and crystal structure of La2Ni7Hx studied by in situ X-ray diffraction. *Inorg. Chem.* **2010**, *49*, 8763–8768.
27. Iwatake Y, Kishida K, Inui H. Crystal Structure Evolution of La_2Ni_7 during Hydrogenation. *MRS Online Proc. Libr.* **2013**, *1516*, 183–188.
28. Zhou H, Yao Q, Yuan S, Liu J, Deng H. Phase relationships in the La–Ni–Si system at 673 K. *J. Alloys Compd*. **2004**, *366*, 161–164.
29. Chen C, Wang X, Huang H, Zou X, Gu F, Su F, et al. Synthesis of mesoporous Ni–La–Si mixed oxides for CO_2 reforming of CH_4 with a high H_2 selectivity. *Fuel Process. Technol.* **2019**, *185*, 56–67.
30. Mayer I, Felner I. High-temperature X-ray study of rare-earth silicides. *J. Less Common Met.* **1972**, *29*, 25–31.
31. Kh R. Surface Properties of Cu Doped La-Ni Intermetallic Compounds. *Chem. Res. Chin. Univ*. **1993**, *9*, 225–230.
32. Kakuta H, Ogawa T, Takamura H, Okada M. Protium absorption properties of La–TM–Si (TM= Co, Ni) ternary intermetallic compounds. *Mater.Trans. JIM* **1998**, *39*, 769–772.
33. Dakka MI, Jain IP. Comparative study of hydrogen in La(28.9)Ni(67.55)Si(3.55) and LaNi5. *Int. J. Hydrogen Energy*. **2000**, *25*, 773–777.
34. Winiarski MJ, Samsel-Czekała M. Electronic structure of the 344-type superconductors La3(Ni; Pd)4(Si; Ge)4 by ab initio calculations. *J. Alloys Compd.* **2013**, *546*, 124–128.
35. Smetana V, Grilli D, Shtender V, Pani M, Manfrinetti P, Mudring AV. La–Ni–Si: A Gold Mine with a Diamond. *Inorg. Chem.* **2024**, *63*, 22761–22770.
36. Sheldrick GM. SHELXT–Integrated space-group and crystal-structure determination. *Found. Crystallogr*. **2015**, *71*, 3–8.
37. Zhang JP, Liao PQ, Zhou HL, Lin RB, Chen XM. Single-crystal X-ray diffraction studies on structural transformations of porous coordination polymers. *Chem. Soc. Rev.* **2014**, *43*, 5789–5814.
38. Lisi N, Dikonimos T, Buonocore F, Pittori M, Mazzaro R, Rizzoli R, et al. Contamination-free graphene by chemical vapor deposition in quartz furnaces. *Sci. Rep.* **2017**, *7*, 9927.
39. *APEX3, SAINT and SADABS, Software for Data Reduction, Absorption Correction and Structure Solution*; Bruker AXS Inc: Madison, WI, USA, 2015.

40. Krause L, Herbst-Irmer R, Sheldrick GM, Stalke D. Comparison of silver and molybdenum microfocus X-ray sources for single-crystal structure determination. *J. Appl. Crystallogr.* **2015**, *48*, 3–10.
41. *XPREP*, V. 2014/2; Bruker AXS Inc: Madison, WI, USA, 2014.
42. Sheldrick GM. Crystal structure refinement with SHELXL. *Cryst. Struct. Commun.* **2015**, *71*, 3–8.
43. Putz H, Brandenburg K. Diamond 4.2.2 Crystal and Molecular Structure Visualization. *Cryst. Impact Kreuzherrenstr.* **2017**, *102*, 53227.
44. Blatov VA, Shevchenko AP, Proserpio DM. Applied topological analysis of crystal structures with the program package ToposPro. *Cryst. Growth Des.* **2014**, *14*, 3576–3586.
45. Liu Y, Fan C, Xu Z, Fu R, Wen B, Zhang L. Orientation Relationship of the Intergrowth $Al_{13}Fe_3$ and $Al_{13}Fe_4$ Intermetallics Determined by Single-Crystal X-ray Diffraction. *Metals* **2024**, *14*, 463.
46. Olcese GL. Crystal structure and magnetic properties of some 7: 3 binary phases between lanthanides and metals of the 8th group. *J. Less Common Met.* **1973**, *33*, 71–81.
47. Raman A. Ternary FeB-and CrB-type phases with yttrium, lanthanum, and some rare earths. *Inorg. Chem.* **1968**, *7*, 973–976.
48. Thompson P, Reilly JJ, Hastings JM. The accommodation of strain and particle size broadening in Rietveld refinement; its application to de-deuterided LaNi5 alloy. *J. Less Common Met.* **1987**, *129*, 105–114.
49. Bodak OI, Gladyshevsky EI, Miskiv MG. Crystal Structure of Ce_2NiSi and related compounds. *Sov. Phys. Crystallogr.* **1972**,*17*, 439–441.
50. Zhang T, Wang K, Huang K, Yao Q, Lu Z, Long QX, et al. Experimental Investigation of Isothermal Section in the La–Ni–Si System at 1073 K. *Intermetallics* **2025**, *179*, 108671.
51. Liu Y, Fan C, Wen B, Xu Z, Fu R, Zhang L. Orientation Relationship of Intergrowth Al_2Fe and Al_5Fe_2 Intermetallics Determined by Single-Crystal X-ray Diffraction. *Metals* **2024**, *14*, 337.